

Original Article

Cite this article: Xing H, Xue C, Zhao X, Symons DTA, and Niu P (2023) Petrogenesis and tectonic implications of the Early Carboniferous shoshonitic to calc-alkaline magmatic rocks of the southern Yili terrane, western Tianshan. *Geological Magazine* **160**: 855–873. <https://doi.org/10.1017/S0016756822001303>

Received: 4 September 2022

Revised: 9 December 2022

Accepted: 14 December 2022

First published online: 4 April 2023

Keywords:


shoshonitic volcanic rocks; slab rollback; tectonic setting; Xinyuan; Yili terrane

Author for correspondence:

Chunji Xue,

Email: chunji.xue@cugb.edu.cn

Petrogenesis and tectonic implications of the Early Carboniferous shoshonitic to calc-alkaline magmatic rocks of the southern Yili terrane, western Tianshan

Hao Xing¹ , Chunji Xue^{2,3}, Xiaobo Zhao², DTA Symons⁴ and Pengqiao Niu¹

¹State Key Laboratory of Nuclear Resources and Environment, School of Earth Sciences, East China University of Technology, Nanchang, Jiangxi 330013, China; ²State Key Laboratory of Geological Processes and Mineral Resource, School of Earth Sciences and Resources, China University of Geosciences, Beijing 100083, China; ³The National 305 Project Office of Xinjiang, Urumqi 830000, China and ⁴School of the Environment, University of Windsor, Windsor, N9B 3P4, Canada

Abstract

In the Yili terrane at Awulale mountain, most shoshonitic lavas are related to post-collision extension and were extruded during the Late Carboniferous to Early Permian (310–280 Ma). Herein, we evaluate a small-volume occurrence of shoshonitic magmas in the southern Yili terrane formed *c.* 346 Ma ago. The high MgO (Mg#) and positive Hf isotope values of the shoshonitic magmas indicate the input of juvenile mantle-derived material. Still, their high Ba–Sr signatures were likely inherited from the partial melting of previously metasomatized lithospheric mantle. We argue the shoshonitic magmatic activity recorded a syn-subduction extensional history in the Yili terrane. This interpretation is consistent with the magmatic records from Early Carboniferous A-type granite and magnesian andesite found in the Zhaosu–Adentao–Dahalajunshan area of the southern Yili terrane. Combined with the geological development in this area, we propose that the emergence of the shoshonitic rocks records either the retreat of the trench or the rollback of the Junggar oceanic slab that occurred at or before the 346.1 ± 3.1 Ma age of the rocks.

1. Introduction

Petrogenetic studies of potassic rocks from several orogenic belts, including the Andes (Kay & Kay, 1993), Tibet (Turner *et al.* 1993) and Sierra Nevada (Manley *et al.* 2000), show that small volumes of K-enriched magmas with arc signatures are genetically related to a minor degree of melting in the sub-continental lithospheric mantle (Turner *et al.* 1993, 1996; Manley *et al.* 2000). Popular tectonic models for the melting of such a lithospheric mantle could include different tectonic settings, such as: (a) asthenospheric upwelling induced by slab break-off during the initial stage of post-subduction collision (Feng & Zhu, 2019); (b) partial convective removal of the sub-continental lithospheric mantle triggered by the shortening and thickening of the continental lithosphere during ongoing continental collisional processes (Turner *et al.* 1996); and (c) rollback and/or foundering of a flat-subducted oceanic plateau in a syn-subduction setting (Li *et al.* 2017). These studies show that the potassic igneous rocks may have huge potential in reconstructing tectonic settings and unravelling mantle enrichment mechanisms.

In recent years, the potassic and shoshonitic rocks have drawn more and more research interest and they are usually regarded as a crucial petrological tool for determining the details of orogenic histories in ancient orogenic belts (Yang *et al.* 2012; Feng & Zhu, 2019). The development of voluminous Phanerozoic magmatic rocks throughout the Central Asian Orogenic Belt (CAOB) provides a rare opportunity to work on such an issue. One of the best-preserved magmatic units in the CAOB is the Devonian–Carboniferous Dahalajunshan Volcanic Formation (DVF) in the Yili terrane (Zhu *et al.* 2005, 2009; Wang *et al.* 2007, 2009; Zhao *et al.* 2014; Huang *et al.* 2020). Specifically, the DVF is an essential marker of subduction of the Palaeozoic oceanic lithosphere beneath the Palaeo-Yili terrane margin (Zhu *et al.* 2009; Huang *et al.* 2020; Xing *et al.* 2021). Recently, however, some researchers have proposed a rift model for the origin of magmatism in the Yili terrane (Xia *et al.* 2012), whereas others have suggested the magmatism resulted from the subduction of an oceanic basin beneath the Yili terrane (Zhao *et al.* 2014; Huang *et al.* 2020). Following recent research, most scholars now accept an active continental margin model, but disagreements remain about the polarity of subduction and the tectonomagmatic origin of the igneous rocks in the Yili terrane. For example, some studies have linked the DVF to the northward subduction of the South Tianshan Ocean (Zhu *et al.* 2005, 2009; Feng &

Zhu, 2020), and other studies to the southward subduction of the Junggar – North Tianshan Ocean (Wang *et al.* 2007, 2009).

The DVF was extruded initially as normal tholeiitic/calc-alkaline (CA) magmas along the northern margin of the Yili terrane (An *et al.* 2013). In contrast, the high-K calc-alkaline (HK-CA) and other alkaline products including the associated shoshonitic basaltic trachyandesite (SHO) magmas of the interior and southern Yili terrane appeared after the Early Carboniferous (Zhu *et al.* 2009; Feng & Zhu, 2019, 2020). Although the Early Carboniferous alkaline magmatic products have been previously found in the southern Xinyuan district (Zhu *et al.* 2005, 2009), the petrogenesis of a shoshonitic series ($\text{SiO}_2 = 52\text{--}54$ wt %, $\text{MgO} > 3$ wt %, $\text{K}_2\text{O} > 3$ wt %) has not been previously reported in this region. Such SHO rocks are important markers of highly metasomatized supra-subduction magma sources. They occur as extrusive bodies with shoshonitic mafic lithologies that show a close relationship to previously erupted calc-alkaline products. This paper reports new field observations, zircon U–Pb ages, major and trace element data, and zircon Hf isotopic dataset for the CA and SHO rocks in the southern Xinyuan region. These findings provide new insights into the significance of the CA–SHO magmatic association in terms of its magmatic source evolution and causative geodynamic processes.

2. Geological background

The Chinese Tianshan is generally divided into the Eastern and Western Tianshan, roughly along longitude 88° E. The Western Tianshan is subdivided into four tectonic units: the North Tianshan, Yili terrane, Middle Tianshan and South Tianshan, from north to south (Fig. 1). The North Tianshan is separated from the Yili terrane and the Middle Tianshan by the North Tianshan Suture formed by the closure of the North Tianshan – Junggar Ocean. The Yili terrane and Middle Tianshan are separated from the South Tianshan by the South Central Tianshan suture (Atbashi–Inylchek Fault) that was formed by the closure of the Turkestan Ocean (the South Tianshan Ocean) (Fig. 1; Windley *et al.* 2007; Zu *et al.* 2019). The Yili terrane forms the eastern part of the Kazakh–Yili microcontinent, beside the easternmost part of North Tianshan (Fig. 1), where it is wedge-shaped toward the western region of Xinjiang, China (Windley *et al.* 2007). The Yili terrane has critical ophiolite-strewn zones along the bounding North Tianshan Fault (or north Boluokenu Fault) on the northern margin and the North Tianshan accretionary wedge on the northern margin. The ophiolites exposed in the Gangou, Mishigou, Luweigou and Bayingou areas represent fragments of the North Tianshan – Junggar oceanic crust. Xu *et al.* (2006) obtained sensitive high-resolution ion microprobe (SHRIMP) U–Pb zircon ages of 324.8 ± 7.1 Ma and 344.0 ± 3.4 Ma from the Bayingou ophiolites (plagiogranite and gabbro). These ages indicate that the North Tianshan – Junggar Ocean existed from the Late Devonian to the Early Carboniferous. Along the southern margin of the Yili terrane is an accretionary wedge that most researchers believe was formed by the northward subduction of the South Tianshan Ocean beneath the Yili terrane. The ophiolites exposed in the Changawuzi, Misibulak–Heiyang Range, Kule Lake and Yushugou areas represent fragments of the South Tianshan Ocean, that have given ages of 450–330 Ma (Long *et al.* 2006). To the north of this ophiolite belt is a high-pressure/low-temperature metamorphic region exposed in the Kekesu–Akeyazi–Atbashi area. The metamorphic activity began before *c.* 345 Ma

and finished by *c.* 300 Ma at the end of the Late Carboniferous, indicating that the Tarim Craton started to collide with the Yili terrane at *c.* 345 Ma at the start of the Early Carboniferous (Gao *et al.* 2006).

The Yili terrane mainly contains a Precambrian basement with overlying Palaeozoic volcanic–sedimentary strata. The basement rocks mainly consist of migmatite, gneiss, amphibolite, schist, quartzite and marble (Wang *et al.* 2014). In the Wenquan area of the NW Yili terrane, Wang *et al.* (2014) obtained a laser ablation – inductively coupled plasma – mass spectrometry (LA-ICP-MS) zircon U–Pb age of 926 Ma from Neoproterozoic migmatites of the Wenquan Group, as well as older, inherited zircons of 980–2500 Ma. In the western part of the Awulale mountain region, JL Li *et al.* (2009) reported a secondary ion mass spectroscopy (SIMS) zircon U–Pb age of 1609 ± 40 Ma from Mesoproterozoic granitic gneisses. The Early Palaeozoic strata are composed of Cambrian to Ordovician siltstone, chert, Silurian neritic clastic sedimentary rocks, carbonate rocks and volcanic rocks (Han & Zhao, 2018). An unconformity separates the Late Palaeozoic rocks from the older strata (XBGMR, 1993). A succession of Late Devonian to Late Carboniferous strata crops out along both sides of the Yili terrane, going upward from the paralic volcanic lava of the Dahalajunshan Formation (DVF) into the neritic clastic rocks and carbonates of the Akeshake Formation, and then into the bimodal volcanic rocks of the Yishijilike Formation (XBGMR, 1993). Permian terrestrial sedimentary and bimodal volcanic rocks unconformably overlie these pre-Permian strata, consisting of the Lower Permian Wulang Formation continental bimodal volcanic rocks and the Upper Permian molasse successions. Granitoid intrusions are also widely emplaced into Devonian to Carboniferous strata that have yielded ages of 362–268 Ma and have primarily arc-like geochemical signatures (Long *et al.* 2011).

The study region is located in the southern part of the Yili terrane, and contains distributed Late Palaeozoic volcanic and sedimentary rocks (Figs 1c, 2 and 3). These rocks are typically in fault contact with, or unconformably cover, Precambrian and Silurian metamorphic rocks. The Late Devonian to Early Carboniferous DVF consists mainly of basalt, andesite, trachyandesite, trachyte and rhyolite with interlayered pyroclastic rocks, sandstone and limestone (Figs 1c, 2 and 3) and ages of 359–324 Ma (Zhu *et al.* 2005, 2009). The early volcanic activity began with the basaltic lava and continued with trachyandesitic to trachytic to rhyolitic lavas and pyroclastic successions. The pyroclastic deposits are mainly tuff and volcanic breccia (Feng & Zhu, 2020). The upper part of the lava–pyroclastic successions is intruded by several granites, mainly consisting of plagiogranite, quartz diorite and diorite (Fig. 2; XBGMR, 1993). To the west of the study region, lava contains primitive CA basalts, A-type granites (354–339 Ma; Li *et al.* 2010) and high-Mg andesite (346 Ma; Wang *et al.* 2020), suggesting that paroxysmal extensional tectonics accompanied the opening of the Wusun–Awulale back-arc basin. The appearance of more potassic lavas in the southern study region validates the extensional tectonic stages of orogenic magmatism, which was confirmed by earlier reports of coeval HK–CA/SHO rocks in the Xinyuan, Laerdundaban and Yuximolegai areas (Zhu *et al.* 2005, 2009; Feng & Zhu, 2019). Shoshonitic rocks, the objects of this study, belong to the early DVF stage of volcanic activity. They are underlain by CA andesitic lava and overlain by andesitic lithic-crystal tuff and andesitic breccia (Fig. 4). Siltstone and sandstone of the Akeshake Formation overlie the DVF and are found in the upper part of this section, where they are in fault contact with the DVF strata. Late Palaeozoic granite plutons intrude the

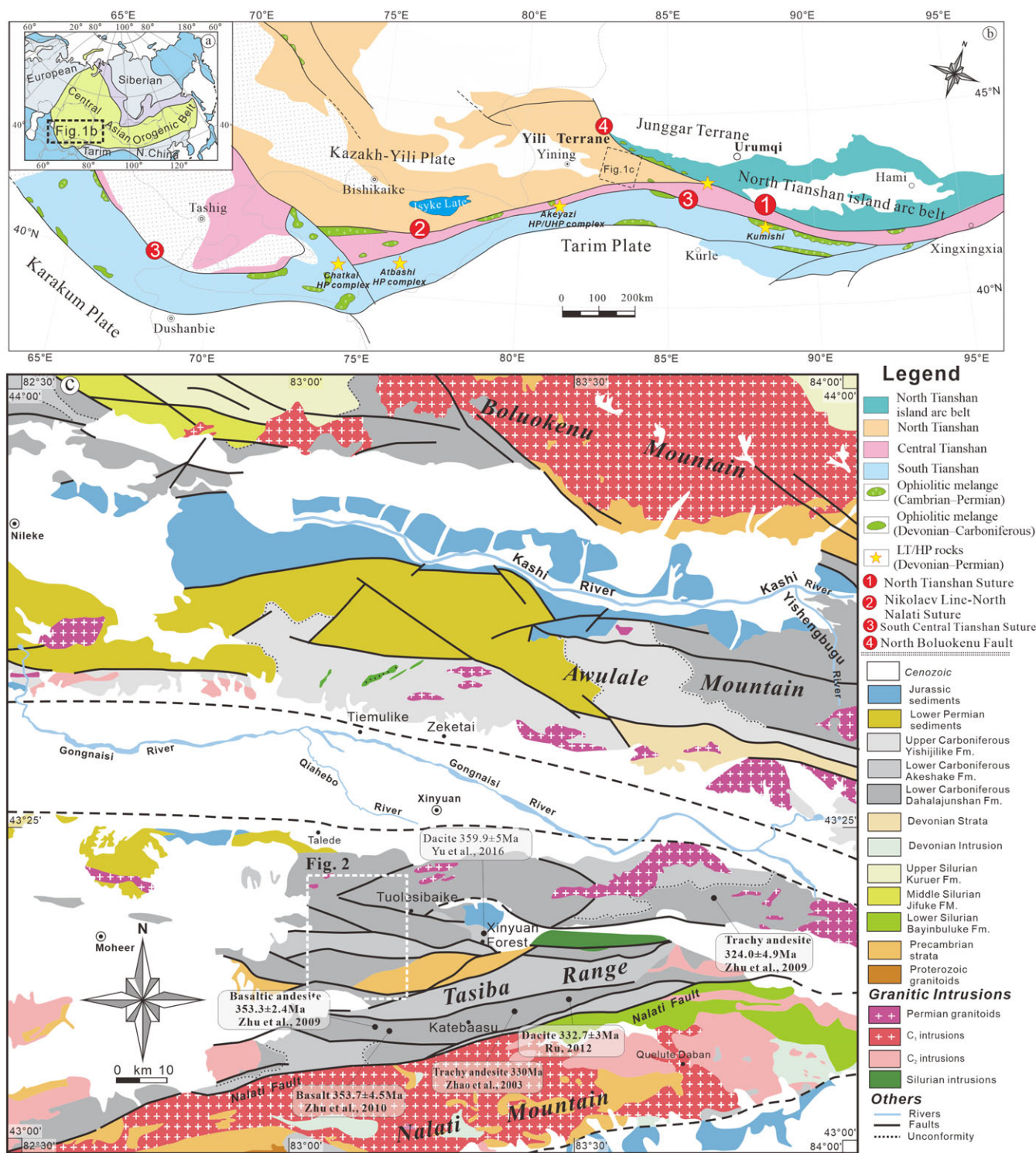


Fig. 1. (Colour online) (a) Tectonic sketch map of the Central Asian Orogenic Belt (CAOB) and its adjacent tectonic units. (b) Sketch map of tectonic units and the location of the Yili terrane in the Tianshan orogeny. (c) Simplified geological map of the Xinyuan, and the SE part of the Yili terrane (modified from 1:250 000 scale geological maps, Xinyuan sheet by XBGMR, 1993). Occurrences of HP/LT rocks according to Tan *et al.* (2019) and Xia & Li (2020).

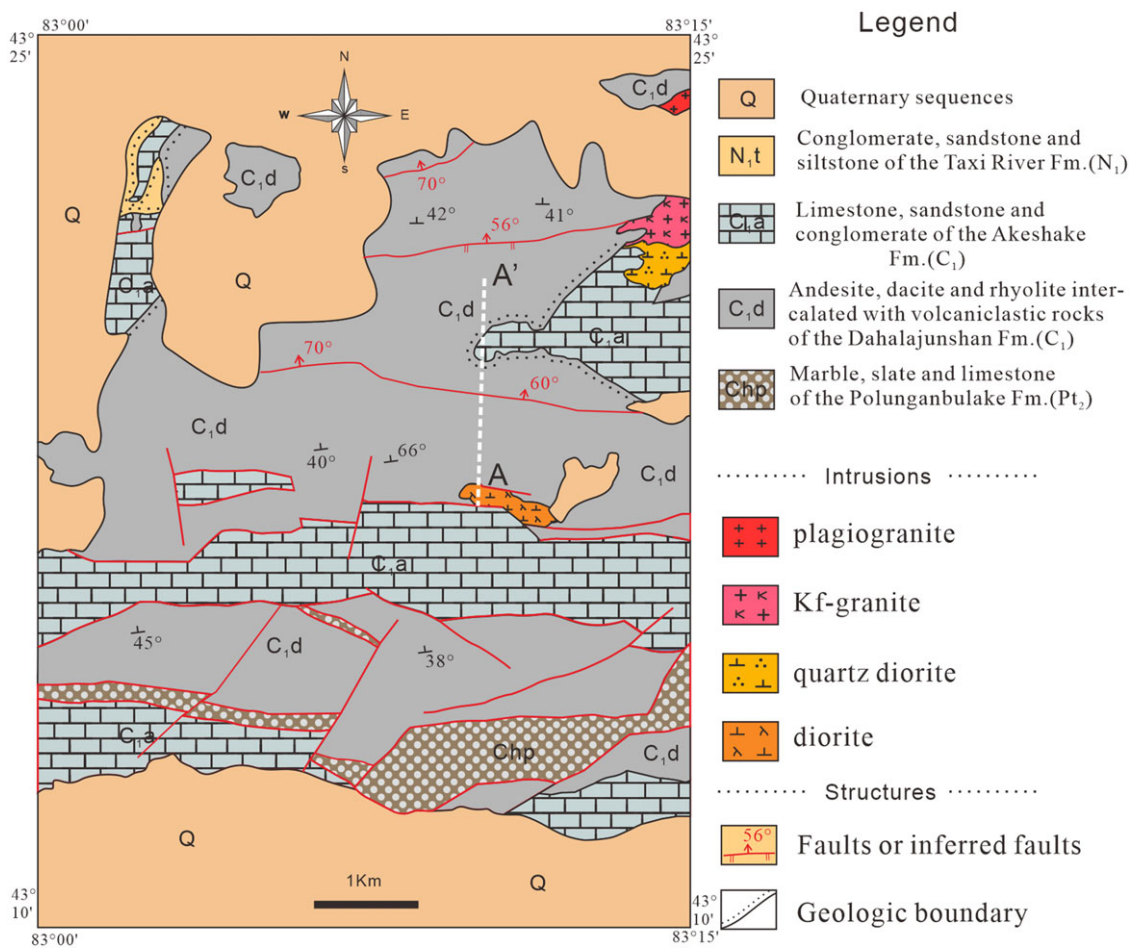


Fig. 2. (Colour online) Simplified map of southern Xinyuan showing the regional geology (modified from XBGMR, 1993). The location of cross-section A–A' in Figure 4 is also shown.

Carboniferous rocks and give a U–Pb zircon date of 318.0 ± 2.3 Ma (XBGMR, 1993). Approximately 10 km east of our study region, Feng & Zhu (2020) also found a granite pluton with a zircon U–Pb age date of 319.4 Ma in the upper part of this lava–pyroclastic succession.

3. Methods

Eight samples (four andesites, four andesitic tuff) were collected for zircon dating and bulk-rock geochemical analysis from the Xinyuan cross-section running between $42^{\circ} 21' 55''$ N, $83^{\circ} 09' 33''$ E– and $43^{\circ} 23' 17''$ N, $83^{\circ} 09' 51''$ E– (Fig. 4). The zircons were separated from a c. 5 kg sample of basaltic trachyandesitic tuff (X10-1) by crushing and sieving. The other samples were crushed and powdered to a 200 μ m size with an agate mortar for bulk-rock geochemical analyses.

3.1 Zircon LA-ICP-MS U–Pb analytical methods

Zircon separation was done using conventional density and magnetic techniques, and the zircons were mounted in epoxy and polished. Photomicrographs were taken under cathodoluminescent (CL), transmitted and reflected light to examine the inner structure and select appropriate test points. Zircon U–Pb isotopic compositions were obtained using a Neptune multiple-collector inductively coupled plasma mass spectrometer (MC-ICP-MS) with a 193nm-

FX ArF excimer laser-ablation system at the Isotopic Laboratory, Tianjin Institute of Geology and Mineral Resources. The laser beam had a spot diameter of 25 μ m, frequency of 10 Hz and energy density of c. 2.5 J cm^{-2} . Helium was used as a carrier gas to enhance the transport efficiency of the ablated materials. GJ-1 was used as an external standard for the U–Pb dating analyses (Jackson *et al.* 2004). Common-Pb corrections were made following Andersen (2002). Nist SRM 610 glass was used as an external standard to calculate U, Th and Pb concentrations of the zircons. Every eight analyses were followed by two analyses of standard zircon GJ-1. Data were processed following Liu *et al.* (2010) and assessed using Isoplot 3 (Ludwig, 2003). Age data and concordia plots are reported with 1σ errors, whereas the uncertainties for the weighted mean ages are at the 95% confidence level. Details of the analytical techniques are described by HK Li *et al.* (2009).

3.2 Whole-rock major and trace element analyses

Major and trace element compositions were analysed by X-ray fluorescence (XRF; Philips PW2404) and ICP-MS (Finnigan MAT-6493, Element 1), respectively, at the Analytical Laboratory of the Beijing Research Institute of Uranium Geology (BRIUG). For the major element analyses, 0.5 g sample powders were mixed with 3.6 g $\text{Li}_2\text{B}_4\text{O}_7$, 0.4 g LiF, 0.3 g NH_4NO_3 and minor LiBr in a platinum pot, then melted to form a glass disc in a high-frequency melting instrument before analysis.

Stratigraphy at Southern Yili terrane

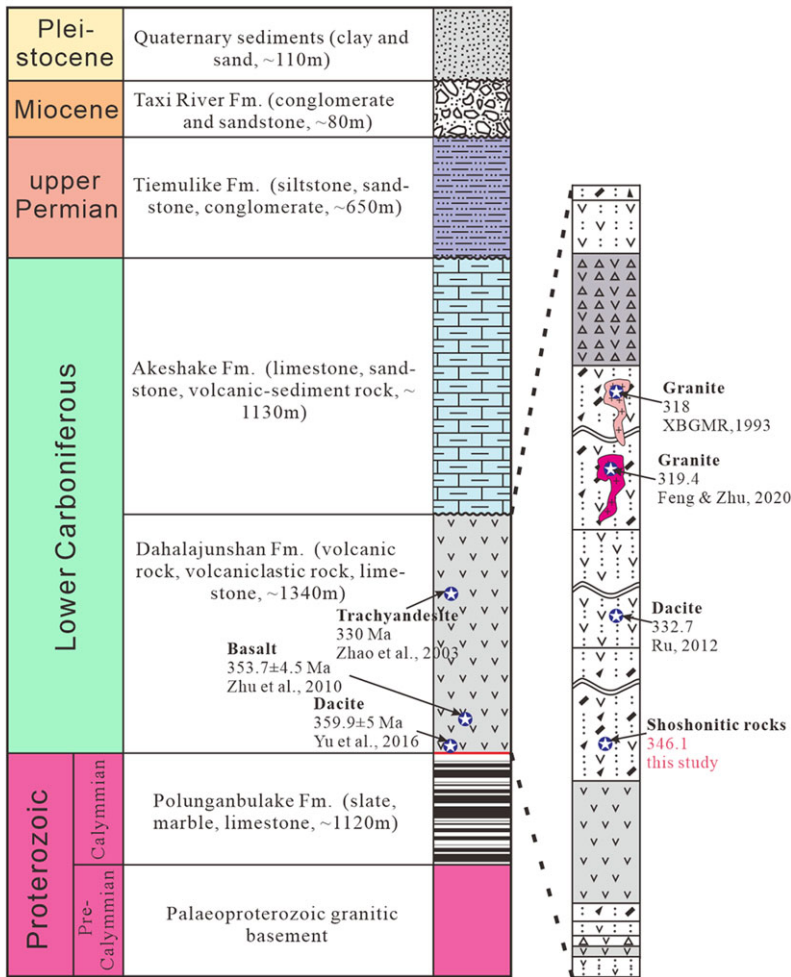


Fig. 3. (Colour online) Typical stratigraphic column diagram for the Xinyuan district members of the Dahalajunshan Formation.

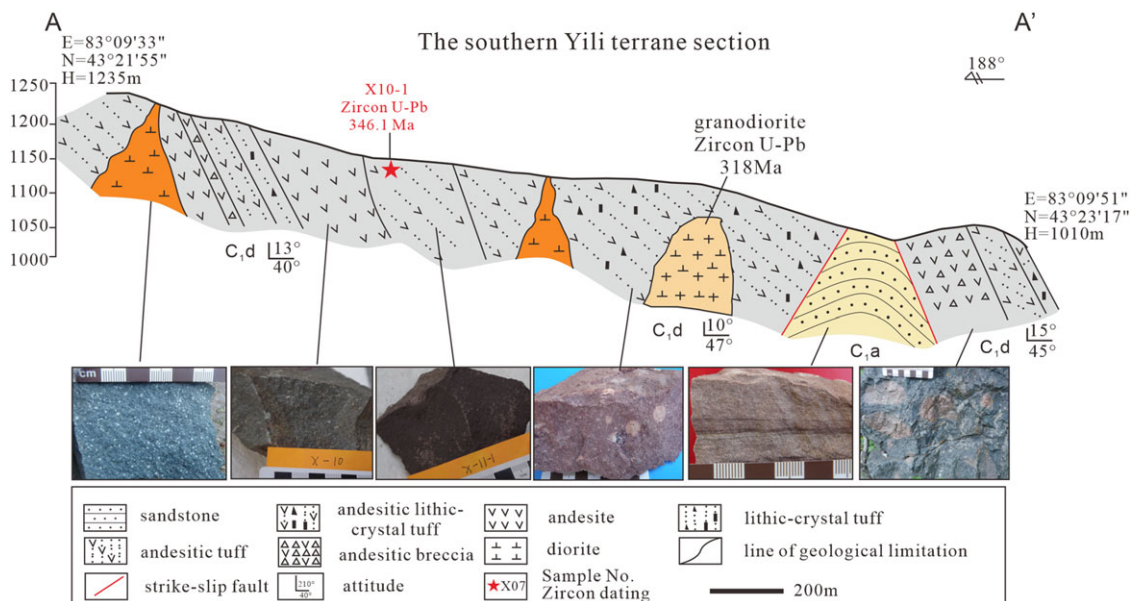


Fig. 4. (Colour online) Cross-section in the southern Xinyuan showing the stratigraphic contact between the late Palaeozoic magmatic rocks and the associated sedimentary rocks. The locations of zircon U-Pb dating samples are also shown.

Major element analytical accuracy is better than 5%. For the trace element analyses (including rare earth), the analytical uncertainties are within 7%. The detailed analytical procedures are described by Cullen *et al.* (2001).

3.3 In situ zircon Lu–Hf isotope analyses

Zircon Hf isotope analyses were carried out *in situ* using a Neptune MC-ICP-MS and a NewWave UP213 ultraviolet laser ablation system at the Institute of Mineral Resources, Chinese Academy of Geological Sciences, Beijing, China. Lu–Hf isotopic compositions were obtained from the same zircon grains previously analysed for the U–Pb isotope analyses using an ablation spot size diameter of 40–80 μm . The analytical procedures and interference correction method of ^{176}Yb on ^{176}Hf are similar to those described by Hou *et al.* (2007). To evaluate the reliability of the analytical data, standard zircon GJ1 was used as reference material. The weighted average $^{176}\text{Hf}/^{177}\text{Hf}$ ratio for the GJ1 zircon standard was $0.282000 \pm 25(2\sigma, n = 26)$. The measured $^{176}\text{Hf}/^{177}\text{Hf}$ ratios and the ^{176}Lu decay rate of $1.867 \times 10^{-11} \text{ yr}^{-1}$ (Söderlund *et al.* 2004) were used to calculate the initial $^{176}\text{Hf}/^{177}\text{Hf}$ ratios. The chondritic values of $^{176}\text{Lu}/^{177}\text{Hf} = 0.282772$ and $^{176}\text{Hf}/^{177}\text{Hf} = 0.0332$ reported by Blichert-Toft and Albarède (1997) were used to calculate the ϵ_{Hf} values.

4. Results

4.1 Petrography and mineral composition of the volcanic rocks

Eight samples from the DVF were collected from southern Yili terrane (Fig. 4; Supplementary Table S2). The samples mainly come from volcanic and volcanoclastic rocks.

4.1.1 Trachyandesite (calc-alkaline series, CA)

Trachyandesites from the southern Yili are greyish green, massive and contain 40–45% phenocrysts of plagioclase, K-feldspar and quartz (Fig. 5d). Hornblende is present in only a few samples. The plagioclase phenocrysts are subhedral and occur as platy columns typically 1.5–2 mm in length and 1 mm in width. Their groundmass is composed of plagioclase, K-feldspar and minor magnetite with a hyalopilitic texture. Plagioclase and mafic minerals in the trachyandesite are commonly replaced by chlorite and calcite.

4.1.2 Basaltic trachyandesitic tuff (shoshonitic series, SHO)

Basaltic trachyandesitic tuffs overlie the trachyandesite in the field, and the tuffs are exposed only in small volumes (Fig. 5a). Fresh basaltic trachyandesitic tuff is purplish-red (Fig. 5b, c) and has a massive texture with 20–35% K-feldspar phenocrysts and 60–70% matrix (Fig. 5f). The K-feldspar phenocrysts are euhedral to subhedral and often exhibit dusty zoning. The phenocrysts occur as platy columns that are typically 1.5–2 mm long and 0.5 mm in width. Their groundmass comprises aphanitic to microcrystalline K-feldspar (0.01–0.05 mm) with minor plagioclase, magnetite and glass (Fig. 5f, g). Opaque minerals (magnetite and ilmenite, up to 5 vol. %) are common in some samples.

4.2 Zircon U–Pb geochronology

Fourteen zircons from basaltic trachyandesitic tuff sample X10-1 were analysed to constrain the crystallization age. Representative CL images of zircon are shown in Figure 6. The zircons from this

sample are prismatic, transparent, stubby and subhedral, with lengths ranging from 80 to 200 μm and widths ranging from 40 to 100 μm , giving length-to-width ratios from 1.5:1 to 2:1. In the CL images, most of these zircon grains display well-preserved concentric oscillatory zoning and some show linear zonation (Fig. 6). Several grains contain inherited cores with luminescence or zircons with brighter CL images (Fig. 6). Most zircons show high Th/U ratios of 0.4–0.9, indicative of a magmatic origin (Hoskin & Schaltegger, 2003). The 14 zircon grains from 14 analytical spots show concordant $^{206}\text{Pb}/^{238}\text{U}$ and $^{207}\text{Pb}/^{235}\text{U}$ results within analytical errors, yielding concordia age of $348.7 \pm 0.76 \text{ Ma}$. This result is consistent with a weighted mean $^{206}\text{Pb}/^{238}\text{U}$ age of $346.1 \pm 3.1 \text{ Ma}$ (MSWD = 0.63). The U–Pb dating results are illustrated in Figure 7 and presented in Supplementary Table S1.

4.3 Bulk-rock geochemistry

Major and trace element compositions of representative samples of the volcanic rocks are given in Supplementary Table S2. The loss-on-ignition is within 3.5 wt% (except for X-12-1 at 4.19 wt%) and shows no apparent correlation with the major or trace elements (Supplementary Table S2), indicating any minor alteration (if present) does not affect the geochemical composition of the whole rock.

4.3.1 Shoshonitic series

High-K to shoshonitic (SHO) rocks contain low SiO_2 contents (52–54 wt%), high alkalis ($\text{K}_2\text{O} + \text{Na}_2\text{O} = 6.64\text{--}7.04 \text{ wt}\%$) and plot in the basaltic trachyandesite field on a SiO_2 vs ($\text{K}_2\text{O} + \text{Na}_2\text{O}$) diagram (Fig. 8c). The SHO rocks are also high in MgO (4.5–6.1 wt%) and tFe_2O_3 (8.9–9.6 wt%). They have Al_2O_3 content of 15.9–16.2 wt%, with A/NK and A/CNK ratios of 1.6–1.7 and 0.9–1.1, respectively, and they belong to the metaluminous to weak-peraluminous series. The SHO rocks show higher K_2O (2.6–3.2 wt%) than other samples and plot in the ‘shoshonitic series’ field on K_2O vs SiO_2 and Na_2O vs K_2O diagrams (Fig. 8a, b). The SHO rocks have high abundances of light rare earth elements (LREE = 83–94 ppm) with $(\text{La}/\text{Yb})_{\text{N}}$ values of 5.1–5.6 and weak Eu negative anomalies ($\delta\text{Eu} = 2\text{Eu}_{\text{N}}/(\text{Sm}_{\text{N}} + \text{Gd}_{\text{N}})$) of 0.90–0.95.

The most striking feature of the SHO rocks is their high Sr and Ba contents (Sr: up to 1537 ppm; Ba: 984 ppm) and relatively low Rb contents (19.6–42.8 ppm) with high K/Rb ratios (320–504) and low Rb/Sr ratios (0.02–0.04) (Supplementary Table S2), which resemble both the high Ba–Sr granitoids as suggested by Tarney and Jones (1994) and the high Ba–Sr rocks from Tibet (Fig. 9; Wang *et al.* 2018). They are also characterized by enriched large-ion incompatible elements and depleted high-field-strength elements (HFSE; Nb, Ta, Ti), thereby showing geochemical features similar to basalts erupted c. 350 Ma in the study region (Fig. 9; Feng & Zhu, 2020). In addition, the SHO rocks have moderate heavy rare earth element (HREE) and Y contents (Yb: 2.4–2.6 ppm; Y: 21–24 ppm), high Sr contents (1194–1537 ppm) and relatively high Sr/Y ratios (52–71) but low La/Yb values (7.2–7.8) that are different from both typical adakites in Awulale and experimental results on partial melting of hydrous basalt in the garnet stability field (Fig. 11d further below).

4.3.2 Medium-K calc-alkaline series

Trachyandesites from the Xinyuan section show high SiO_2 (57–58 wt%) and alkalis ($\text{K}_2\text{O} + \text{Na}_2\text{O} = 7.4\text{--}7.5 \text{ wt}\%$), and plot in the fields of trachyandesite or andesite on a SiO_2 vs ($\text{K}_2\text{O} + \text{Na}_2\text{O}$) diagram (Fig. 8c). These rocks have low K_2O (1.2–1.5 wt%),

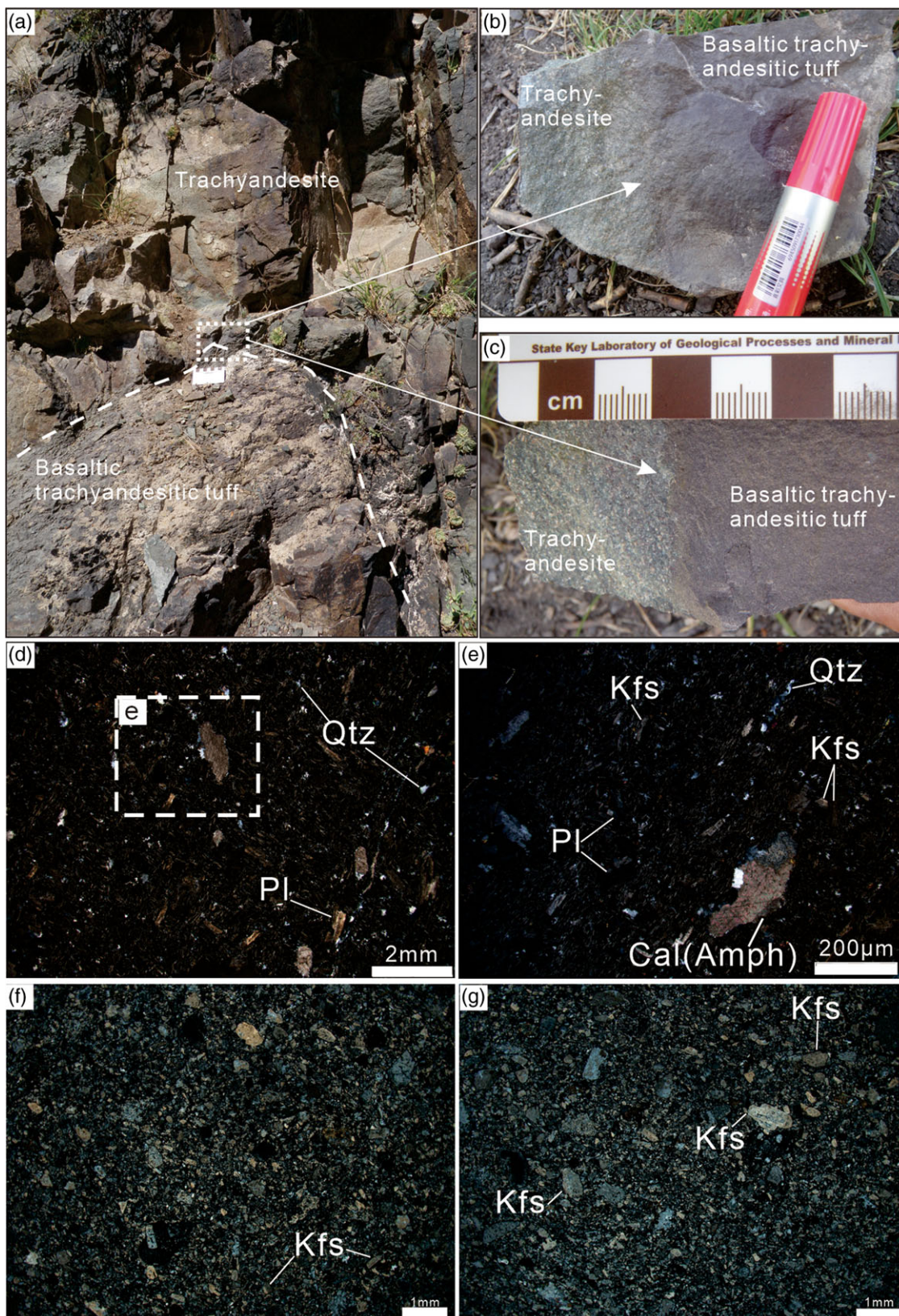


Fig. 5. (Colour online) Microscopic pictures of the Early Carboniferous volcanic rocks in the southern Xinyuan. (a) Field occurrences of the CA andesite and basaltic trachyandesitic tuff. (b, c) Field contact between the CA andesite and the basaltic trachyandesitic tuff. (d, e) Microscopic photos for the CA andesite. (f, g) Microscopic photos for the basaltic trachyandesitic tuff. Abbreviations: Kfs = K-feldspar; Pl = plagioclase; Qtz = quartz; Cal = carbonate; Amph = amphibolite.

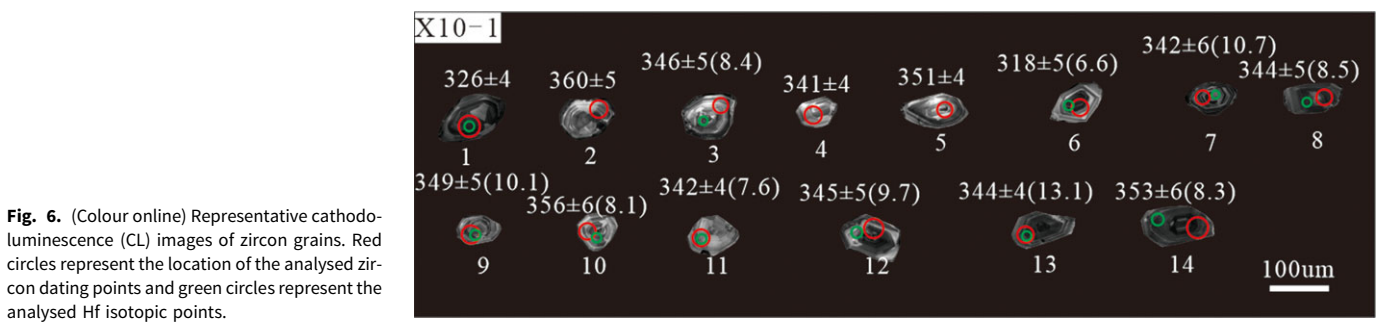


Fig. 6. (Colour online) Representative cathodoluminescence (CL) images of zircon grains. Red circles represent the location of the analysed zircon dating points and green circles represent the analysed Hf isotopic points.

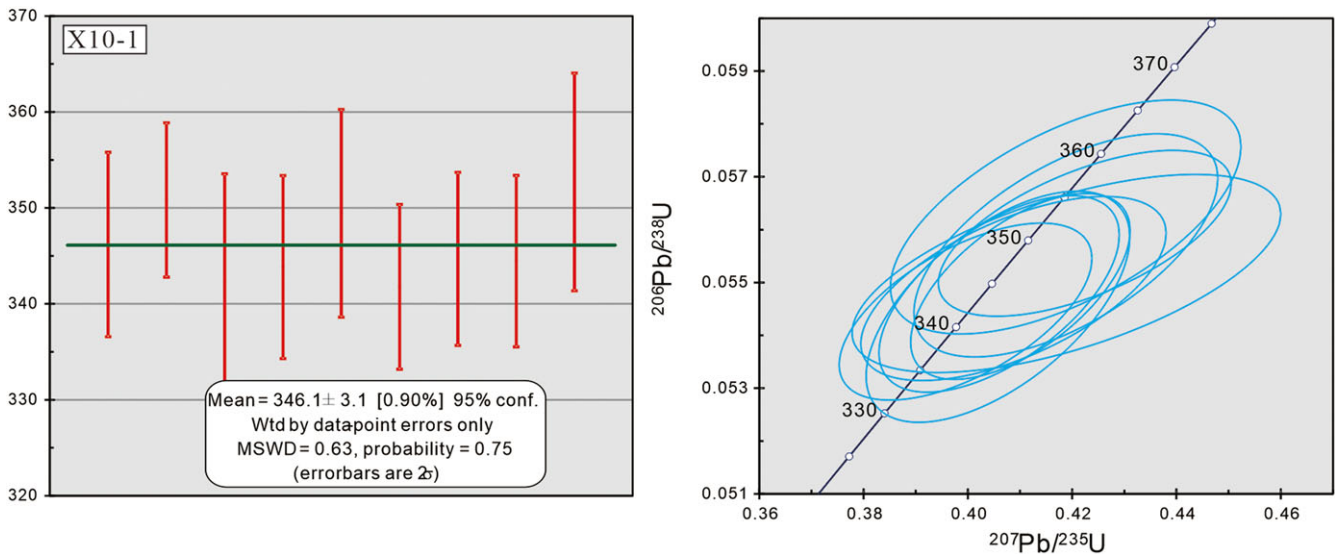


Fig. 7. (Colour online) Weighted average age of the zircon grains in the studied volcanic rock (left panel); LA-ICP-MS U–Pb zircon concordia diagram (right panel).

MgO (2.4–2.9 wt %) and $t\text{Fe}_2\text{O}_3$ (7.7–8.1 wt %) contents. They contain Al_2O_3 (16.9–17.2 wt %) with A/NK and A/CNK ratios of 1.5–2.8 and 0.9–1.0, respectively, and they belong to the metaluminous series. These trachyandesitic samples plot in the medium-K calc-alkaline (CA) series field on SiO_2 vs K_2O and K_2O vs Na_2O diagrams. The total REE and other trace elements of andesites from the Xinyuan section are similar to the SHO rocks, but they show either no Eu anomalies or weakly positive ones of 0.99–1.02. Also, these CA rocks show relatively low contents of LREE (80–87 ppm) with $(\text{La}/\text{Yb})_{\text{N}}$ ratios of 2.4–2.6 and low concentrations of HFSE, and low P and Ti in their trace element patterns. One sample (X12), also collected from the same rock section, shows very different geochemical characteristics, with low SiO_2 (51 wt %) and alkalis ($\text{K}_2\text{O} + \text{Na}_2\text{O} = 4.5$ wt %). X12 plots in the basaltic andesite field on a SiO_2 vs $(\text{K}_2\text{O} + \text{Na}_2\text{O})$ diagram (Fig. 8c). This sample has high contents of K_2O (1.65 wt %), MgO (4.84 wt %) and $t\text{Fe}_2\text{O}_3$ (10.12 wt %), and a lower total REE content than the other trachyandesites. However, its trace elemental pattern is similar to the basalt from Xinyuan and to the SHO rocks in this study (Fig. 9).

4.4 Zircon Hf isotope data

Zircon Hf isotopic analyses were conducted on the same samples used for U–Pb dating. The zircon Hf isotopic data from the volcanic samples are illustrated in Figure 6 and (further below) Figure 11c and listed in Supplementary Table S3. All the results

of the analysis show a positive variation in initial Hf isotope composition, with mantle-like $\epsilon_{\text{Hf}}(t)$ values (+7.6 to +13.1) and very young one-stage model ages (T_{DM}) of 457–678 Ma.

5. Discussion

5.1 Relationship between the medium-K calc-alkaline andesite (CA) and the basaltic trachyandesitic tuff (SHO)

The CA and SHO have a close temporal–spatial relationship in the field (Fig. 5). As the CA rocks are lower in the stratigraphic section, we tentatively consider that the CA erupted slightly earlier than the SHO rocks. However, higher SiO_2 contents and lower concentrations of Al_2O_3 and trace elements (such as the LREE) in the CA relative to SHO rocks suggest that the two rock types were not derived from the same magma. Further, the absence of a noticeable Eu anomaly in the more evolved CA rocks cannot be explained by fractional crystallization from the same parental magma. In addition, the evolutionary path of SHO follows a linear trend of similar or higher K content (Beccaluva *et al.* 2013), but the CA rocks have no such characteristics (Fig. 8a). It is generally accepted that an evolved CA magma should contain higher concentrations of large-ion lithophile elements (LILEs; e.g. K, Ba and Sr) and lower concentrations of compatible elements (e.g. Cr and Ni) relative to an unevolved SHO magma if they originated from a common parental magma. In the present case, however, the SHO rocks have higher contents of K_2O , LILEs (e.g. Sr, Ba; Fig. 9) and other

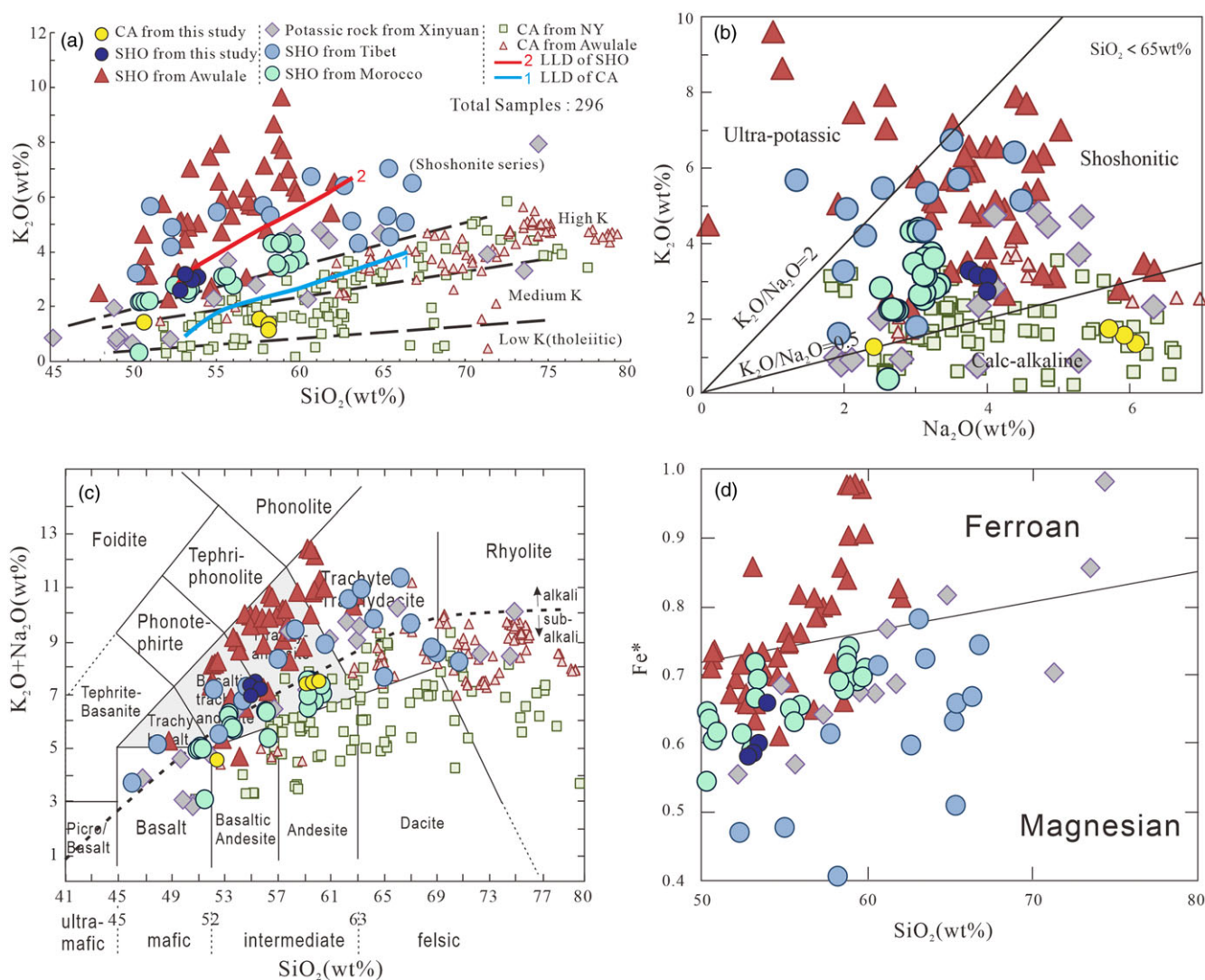


Fig. 8. (Colour online) Comparison of the geochemical characteristics between the calc-alkaline, shoshonite association rocks and shoshonitic rocks from this study in (a) K_2O vs SiO_2 diagram; (b) K_2O vs Na_2O diagram (Turner *et al.* 1996); (c) total-alkali silica (TAS) diagram; and (d) Fe^* vs SiO_2 diagram. Data sources: the Awulale shoshonite database (Yang *et al.* 2012; Feng & Zhu, 2019); the Xinyuan potassic rocks (Zhu *et al.* 2009); the CA rocks from North Yili (Long *et al.* 2006, 2011; Wang *et al.* 2007; Xia *et al.* 2012; An *et al.* 2013); CA from Awulale (Long *et al.* 2011; Huang *et al.* 2020); the Tibet shoshonite rocks (Campbell *et al.* 2014); the Morocco shoshonite rocks (Gill *et al.* 2004). Abbreviations: SHO = shoshonite series, CA = calc-alkaline series.

incompatible elements (e.g. LREE) than do the CA rocks. Therefore, it is implausible that the SHO and CA rocks in the study region are the evolved products of a single magma. For these reasons, we tentatively consider that the CA and SHO series rocks evolved from different parental magma.

5.2 Petrogenesis of medium-K calc-alkaline andesite (CA) and shoshonitic basaltic trachyandesitic tuff (SHO)

The CA rocks contain hornblende and plot in the metaluminous field with $A/CNK < 1.1$ (Table S2), low K_2O/Na_2O ratios (mostly < 1) and low to moderate $Mg\#$ values (33–58) that range across the lower-crust – mantle boundary of 40 (Rapp & Watson, 1995), which indicates that they are I-type magmatic rocks (Chappell, 1999). The rocks have arc-affinity trace element compositions characterized by enrichment in LILE and LREE relative to HFSE (Nb, Ta) with strongly positive Pb and negative Ti anomalies. Their geochemistry is similar to most calc-alkaline magmas found

in the adjacent region, probably formed in a continental arc setting (Fig. 9a, b; Zhu *et al.* 2005, 2009). Previous studies have suggested that CA rocks are formed in a continental arc setting and derived from: (1) an evolved melt derived from the differentiation of an arc-like basaltic parental magma (Lee & Bachmann, 2014); (2) the partial melting of subducted oceanic mafic crust or sediment with subsequent melt–peridotite interaction (Saunders *et al.* 1987); (3) the partial melting of the lower crust during delamination, wherein the resultant melt interacts with mantle peridotite (Kay & Kay, 1993); and (4) the partial melting of metabasalts (amphibolites) in the lower crust from the intrusion of mantle-derived magmas (Petford & Atherton, 1996). In general, the fractional crystallization of an arc-like basaltic parental magma produces an evolved melt that possesses an Eu anomaly and a high content of incompatible elements such as Ba and Rb. Most of the CA rocks have relatively high SiO_2 and low MgO, Ni and Cr contents with the exception of one sample (X-12), which had lower SiO_2 and higher MgO, Ni, Cr, Rb and Ba contents and a minor Eu

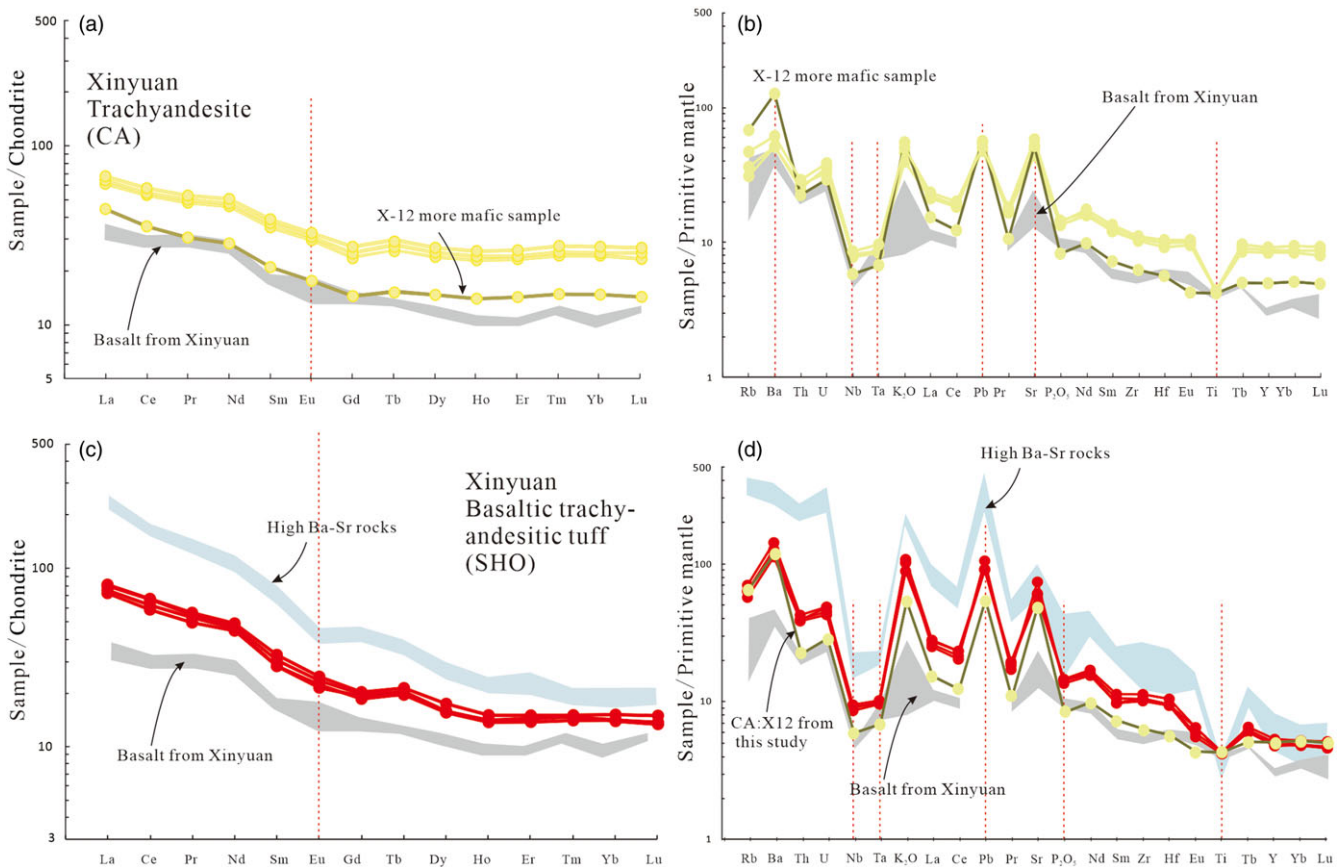


Fig. 9. (Colour online) Chondrite-normalized REE patterns (left) and primitive-mantle-normalized multiple trace element diagrams (right). The chondrite values are from Taylor & McLennan (1985). The primitive-mantle values are from Sun & McDonough (1989). Data for the high Ba-Sr are from Wang *et al.* (2018), and data for the Xinyuan Basalt are from Feng & Zhu (2020).

anomaly. Therefore, if the high-SiO₂ CA rocks evolved from a melt similar to that of X-12, they should have a negative Eu anomaly and a higher content of incompatible elements. However, the CA rocks herein either showed a weak or no Eu anomaly and lower contents of the incompatible elements than the more mafic X12 sample (Fig. 9a, b). This cannot be explained via the fractional crystallization and differentiation of a parent mafic magma. Instead, it requires that the andesitic to dacitic adakitic magmas formed via subducted oceanic slab melt interact with mantle wedge peridotite to produce the high bulk Mg#, Ni and Cr for a given SiO₂ content during ascent (Kelemen *et al.* 2003). However, the CA rocks herein have high SiO₂ and low Mg# values (Fig. 10a, b), indicating that they were not in equilibrium with mantle peridotite. The delamination model of the lower crust could also be excluded because of delaminated lower-crust melt inevitably interacting and equilibrating with the mantle peridotite. The geochemical characteristics of our samples suggest that models (2) and (3) are not suitable for generating these CA rocks. Moreover, the CA rocks have low molar Al₂O₃/(MgO + FeO^T) ratios, relatively high molar CaO/(MgO + FeO^T) ratios (Fig. 10d) and they plot in the field of metabasaltic and eclogite experimental melts on the Mg# and MgO vs SiO₂ diagrams (Fig. 10a, b), whereas the more mafic X12 sample plots near the mantle melts region. Furthermore, from thermal modelling, Dufek and Bergantz (2005) found that the aluminium saturation index for the CA rocks is distributed along the dehydration melting line of amphibolite under moderate to high pressure.

Their experimental results indicate that the CA samples were probably derived from the partial melting of amphibolite by underplated juvenile mafic material. Regarding the trace elements, three samples in this study show either no or only a tiny positive Eu anomaly on the characteristic listric-shaped REE profile of the chondrite-normalized diagrams, which implies that the melt probably coexisted with amphibole. In contrast, the more mafic X-12 sample shows high Sr/Y ratio, low SiO₂ content and high MgO (Mg#) content, indicating that it was formed at a greater depth and had a more juvenile source material. Moreover, all of the CA samples exhibit a flat HREE (Ho to Lu) pattern, suggesting that they were derived from a typical continental lower crust, rather than under high-pressure conditions with garnet as the primary residue (Castillo *et al.* 1999). Therefore, the underplating mafic magma was likely metamorphosed at depth to meta-amphibolite. The subsequent partial melting of the meta-amphibolite at the crust–mantle interface and its subsequent evolution account for the geochemical signature of the CA rocks in the southern Xinyuan region.

The Early Carboniferous SHO rocks in Xinyuan are different from the CA samples. They have higher Na₂O and K₂O and lower CaO and TiO₂ contents, likely due to the presence of alkali-feldspar. In particular, the SHO samples have low SiO₂ (52–54 wt %), high MgO (4.5–6.1 wt %; Mg# = 48–57) and high K₂O contents (2.6–3.2 wt %), which means that they are low-SiO₂ shoshonitic rocks (Fig. 8) as defined by Morrison (1980). Generally, the input

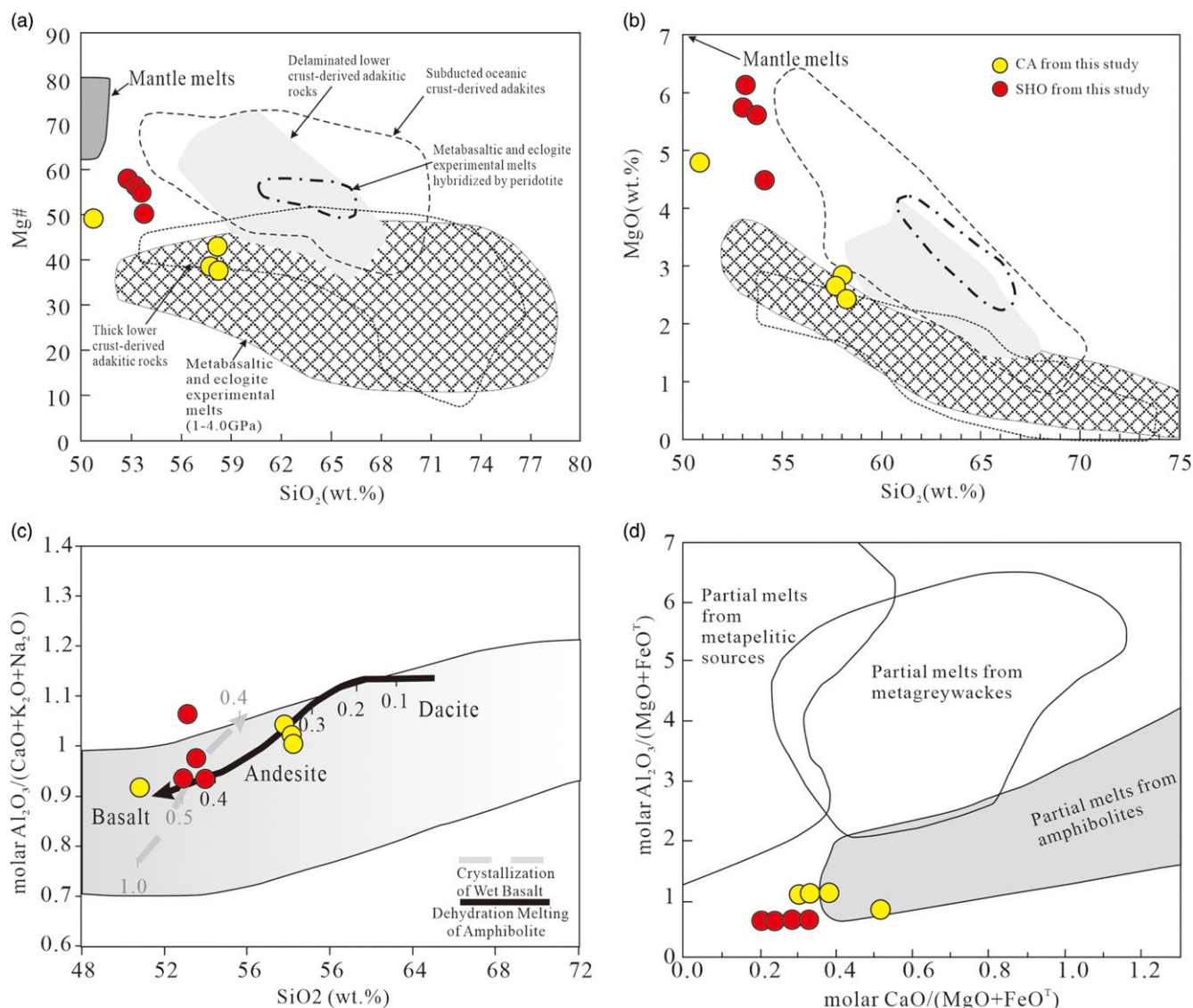


Fig. 10. (Colour online) (a) Mg number vs SiO₂ (wt %) diagram for the Xinyuan samples. (b) MgO (wt %) vs SiO₂ (wt %) diagram for the Xinyuan samples. The field for adakites derived from slab melting is from Defant & Kepezhinskas (2001), for metabasaltic and eclogite experimental melts is from Rapp and Watson (1995), and for metabasaltic and eclogite experimental melts hybridized by peridotite is from Rapp and Watson (1995). (c) Aluminium saturation index (ASI) vs SiO₂ (wt %) for the partial melts of dehydrating amphibolite and fractionating wet basalt. The curves have melt fractions indicated by black for amphibolite dehydration and grey for the wet basalt. This diagram is modified after Dufek & Bergantz (2005). Also shown is the ASI range of calc-alkaline magmas (shaded area). (d) Molar Al₂O₃/(MgO + FeO^T) vs molar CaO/(MgO + FeO^T). Fields of the partial melts were obtained in experimental studies by dehydration melting of various bulk compositions by Altherr *et al.* (2000).

of subducted material into a mantle wedge can produce vein networks of amphibole and phlogopite within the sub-continental lithospheric mantle (Foley 1992). Interactions between these metasomatic veins and mantle magmas will subsequently result in the formation of both SHO and CA rocks (Avanzinelli *et al.* 2009). The popular petrogenesis model for the SHO magmas can be summarized as follows: (1) partial melting of mafic lower crustal rocks (Pe-Piper *et al.* 2009), and (2) partial melting of the metasomatized sub-continental lithospheric mantle (SCLM) with minor fractional crystallization (Campbell *et al.* 2014).

Previous experimental data demonstrate that the partial melting of basaltic igneous rocks can produce metaluminous to weakly peraluminous rock signature. The resultant magmas are generally calc-alkaline to high-potassium calc-alkaline (Rapp & Watson, 1995). With an increasing initial potassium composition in the source rock, small amounts of partial melting of a mafic source

in the lower crust can produce more potassium to make dacitic to rhyolitic compositions (Sisson *et al.* 2005). For example, Pe-Piper *et al.* (2009) proposed that some SHO rocks could be formed by the partial melting of K-enriched basaltic rocks under high-pressure (1.5–2.0 GPa) and high-temperature (950 °C) conditions. However, SHO rocks formed by this mechanism are expected to have geochemical features similar to those of adakitic rocks (Pe-Piper *et al.* 2009). Adakitic rocks are characterized by high Sr/Y (>20–40) and La/Yb (>20) ratios and low Y (≤18 ppm) and Yb (≤1.9 ppm) contents as a result of the presence of garnet and/or amphibole residues in the source (Defant & Kepezhinskias, 2001). In this study, however, the SHO samples have relatively high contents of Y and Yb (21–24 ppm and 2.4–2.6 ppm, respectively), La/Yb ratios of less than 10 (Supplementary Table S2), and high Sr/Y ratios, which are probably due to the extremely high Sr content in the rocks. In a diagram of Sr/Y vs Y, the SHO samples plot outside

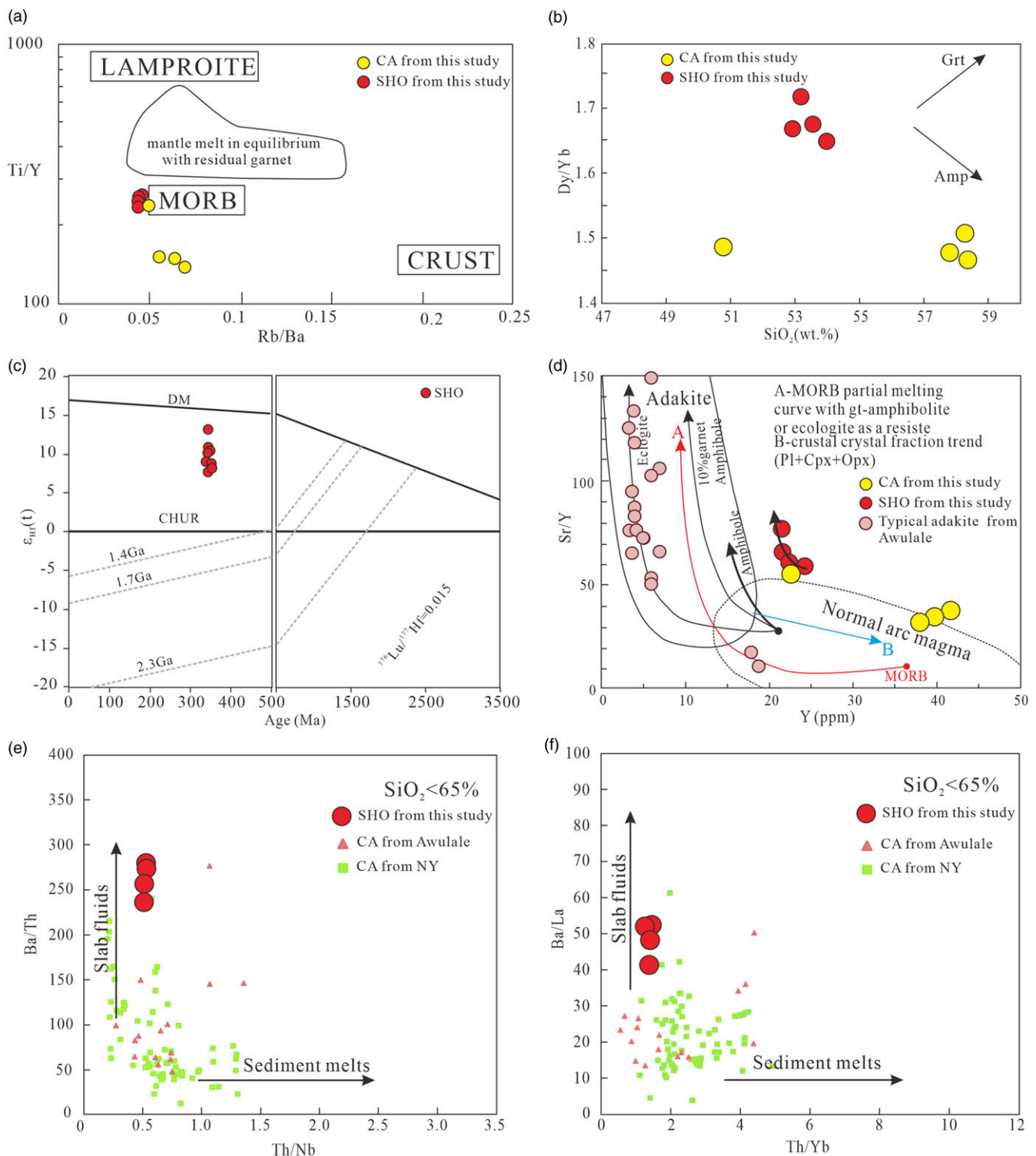


Fig. 11. (Colour online) Geochemical plots for the SHO and CA from this study. (a) Ti/Y vs Rb/Ba diagram shows that the elemental composition of the SHO and CA samples (especially for sample X12) is more akin to MORB and different from crustal-derived magmas. (b) Dy/Yb vs SiO₂. (c) Hf isotopic evolution diagram with the initial ¹⁷⁶Hf/¹⁷⁷Hf values calculated using the respective crystallization ages of the SHO samples. (d) Sr/Y vs Y diagram. (e) Ba/Th vs Th/Nb diagram. (f) Ba/La vs Th/Yb diagram. Data of typical adakite from Awulale Mountain is from Huang *et al.* (2020), and data of CA (SiO₂ < 65%) from Awulale and NY are from Long *et al.* (2006, 2011), An *et al.* (2013), Zhao *et al.* (2014) and Huang *et al.* (2020). Mineral abbreviations: Amp = amphibole, Grt = garnet.

the region of adakite, and their distribution is different from that of a typical adakite of the Awulale mountain region (Fig. 11). Moreover, experimental studies have indicated that magmas generated by the partial melting of mafic crustal rocks generally have Mg# value below 40 (Rapp & Watson, 1995). Meanwhile, the SHO

rocks in this study are characterized by low SiO₂ and high MgO contents, coupled with relatively high Mg# (48–57) and transition element contents (e.g. V = 170–210 ppm, Cr = 133–169 ppm). Note that the high Sr (1194–1537 ppm) and Ba (774–984 ppm) contents of these SHO rocks cannot be produced by the melting

of the juvenile mafic lower crust only. Therefore, it is unlikely that these samples were formed by the partial melting of basaltic igneous rocks in the lower crust.

An alternative model that could explain the formation of the high-K magmatic rocks in the study area is the minor degree melting of the enriched SCLM. Except for fluid-mobile elements such as Rb, Ba and Sr, the Xinyuan SHO rocks in the DVF have geochemical characteristics (i.e. major and trace elements, Hf isotopes) that are similar to those of the basaltic and potassic rocks from the SCLM in this region (Fig. 9 c, d; Zhu *et al.* 2009; Feng & Zhu, 2020). This similarity, as well as their high K₂O, Ba, Sr contents and mantle-like $\epsilon_{\text{Hf}}(t)$ values (+7.6 to +13.1), suggests that both mantle-derived and alkali-rich melts contributed to their high-K magmatic parental melt. Moreover, these SHO rocks exhibit arc-like signatures, including enriched LILEs and negative Ti, Nb and Ta anomalies. However, they differ from typical arc magmatic rocks by having small to no Zr and Hf anomalies (Fig. 9d) typical of magmatic rocks derived from extensional environments because peralkaline melts increase the solubilities of Zr and Hf (Collins *et al.* 1982). Further, the high Ti/Y and low Rb/Ba ratios are not generally ascribed to the continental crust (Fig. 11a). The compositions have suffered neither severe crustal contamination nor equilibrium with a mantle-derived melt having residual garnet. Instead, these features indicate a close relationship with a mid-ocean ridge basalt (MORB)-like melt.

Previous experiments have shown that fluids in equilibrium with eclogitized altered oceanic crust and sediments can carry thousands of parts per million of Sr and Ba. Thus they can substantially elevate the Sr and Ba contents in the overlying lithospheric mantle (Hermann & Rubatto, 2009). This observation is supported by studies from magmas in subduction zones (Vigouroux *et al.* 2008) and primitive melt inclusions in arc rocks (Portnyagin *et al.* 2007). Therefore, we infer that the high MgO (Mg#), Sr and Ba contents were derived from melting of the SCLM that had been metasomatized by fluids released from an earlier subduction process. Although the SHO is closely related to the mantle, their MgO, Mg# values are lower than those of the mantle melt (Fig. 10a, b), meaning that they were not formed directly from the partial melting of the mantle source. Instead, the decrease in tFeO, CaO, MgO, Cr and Ni contents with increasing SiO₂ suggests that the SHO rocks are derivatives from more mafic sources via minor fractional crystallizations of olivine, clinopyroxene and/or plagioclase.

Castro *et al.* (2013) suggested that K-enriched magmas may be generated from a previously metasomatized mantle source when triggered by change in temperature and pressure and/or by increased infiltration of volatile-rich fluids released from the subducted slab. The Ba/Th and Ba/La ratios for the SHO rocks range from 235 to 276 and 41 to 52, respectively, which exceed those of most of the coeval CA series in the Yili terrane (Fig. 11e, f), suggesting that an abundance of hydrous minerals, amphiboles or phlogopites existed in the source region. Further, the $\epsilon_{\text{Hf}}(t)$ values of the zircons in the SHO rocks show positive variable distributions ($\epsilon_{\text{Hf}}(t) = +7.6$ to +13.1) and very young $T_{\text{DM}} = 457$ –678 Ma, which suggest that they were probably derived from a previously short-lived metasomatized lithospheric mantle. Owing to the strong affinity of HREE in garnet and the moderate affinity of middle rare earth elements (MREE) in amphibole, garnet fractionation from the melt should yield increasing LREE/MREE (e.g. (La/Sm)_N) and MREE/HREE (e.g. (Dy/Yb)_N) ratios. In contrast, amphibole fractionation should yield an increasing LREE/MREE ratio, and a nearly constant or decreasing MREE/HREE

ratio (Richards & Kerrich, 2007). In a Sr/Y vs Y diagram, the SHO rocks distribute sub-parallel to the mafic amphibole source melting trendline and their K-enrichment (high K/Rb ratio) indicates that amphibole is a primary residual mineral phase in the source. These same tendencies are also seen in a Dy/Yb vs SiO₂ diagram (Fig. 11b). On a La vs La/Sm diagram (Fig. 12b), the partial melting trajectories that coincide with the SHO samples imply c. 7–8% partial melting of an enriched spinel lherzolite source, which is consistent with the melting degrees of the adjacent Early Carboniferous basaltic (Feng & Zhu, 2020) and Late Carboniferous basaltic andesite samples (Yang *et al.* 2012). These features indicate that the SHO rocks in the southern Yili terrane were most likely derived from partial melting of a previously metasomatized lithospheric mantle source that underwent minor fractional crystallization during ascent towards the surface.

5.3 Implications for the Late Palaeozoic tectonic evolution of Yili terrane

Typical potassic magmatic rocks have been documented in orogenic belts worldwide. Still, they are also found in other tectonic settings such as post-orogenic (Bonin, 2004), intraplate (Wang *et al.* 2014) and active subduction margins (Morrison, 1980) where their emergence suggests an extensional tectonic regime. In contrast, many examples of the SHO association show an intimate relationship with a tholeiitic to CA association in an evolved orogenic tectonic setting where the SHO rocks tend to be younger and to occur above a deeper part of the Benioff zone that is further away from the oceanic trench (Morrison, 1980).

K-enriched magmas in the Yili terrane belong to two eras, i.e. 350–340 Ma (Early Carboniferous; Zhu *et al.* 2005, 2009; this study) and 310–280 Ma (Late Carboniferous to Early Permian; Yang *et al.* 2012; Feng & Zhu, 2019), as shown in Figure 13. Many authors have interpreted the late-stage K-enriched magmatism to have originated from the break-off of the subducted slab after the closure of the Junggar or South Tianshan ocean (Yang *et al.* 2012; Feng & Zhu, 2019). However, the petrogenesis of the Early Carboniferous K-enriched magmatism remains poorly understood. Previous studies have implied the presence of an extensional setting in the Yili terrane during the Early Carboniferous. For example, in the Zhaosu and Adenta regions, there are coeval Fe–Ti basalts, A-type granites (354–339 Ma; Li *et al.* 2010) and high-Mg andesites (346 Ma; Wang *et al.* 2020), which suggest the presence of a back-arc extensional environment in an active continental margin. In this study, the SHO series in Xinyuan was extruded at c. 346 Ma. Their detailed geochemical features indicate that the SHO rocks are most likely the evolved product of a parent magma derived from the melting of metasomatized sub-continental mantle rocks. Nevertheless, it is still unclear whether the SHO rocks were formed in a subduction-related environment or a post-collisional period caused by the partial melting of the sub-continental lithospheric mantle.

Based on the occurrence of Devonian–Carboniferous intrusions and coexisting A-type granites distributed along its southern margin, some authors have proposed that the Yili terrane's late Palaeozoic magmatic activity was generated in a post-collisional setting of the South Tianshan oceanic crust (Xu *et al.* 2013). However, this model is inconsistent with published data and observations. For example, there are no known Early Carboniferous adakitic rocks in the southern Yili terrane as would be expected to result from the melting of a broken slab (Omran *et al.* 2008). Also, slab break-off would have induced a linear heat pulse parallel

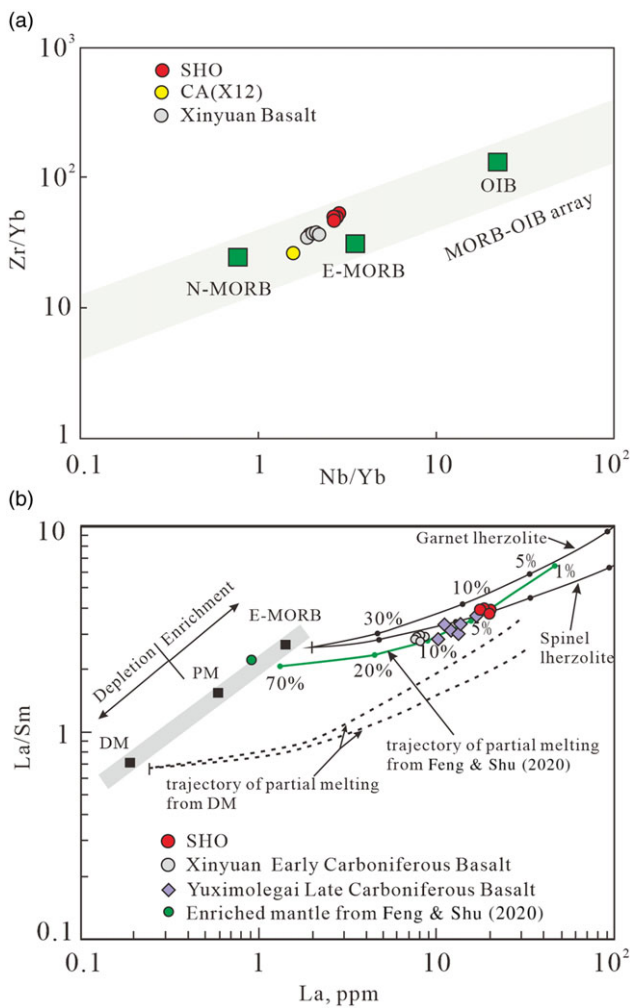


Fig. 12. (Colour online) Plot of (a) Zr/Yb vs Nb/Yb for the SHO and CA samples from the Xinyuan region. The basalt samples are from Feng & Zhu (2020). Normal MORB (N-MORB), enriched MORB (E-MORB) and ocean island basalt (OIB) are from Sun & McDonough (1989). (b) Plot of La vs La/Sm for the SHO samples in this study, showing the partial melting degrees of the Early Carboniferous mantle in the Xinyuan region; the green mantle melting line is from Feng & Zhu (2020) (for other details see Zhu *et al.* 2009).

to the subduction zone, which would have produced a relatively narrow linear zone of magmatism that is not present (Keskin *et al.* 2008). Only the Awulale magmatic belt exhibits a linear zone, but the ages of its magmatic events are later than the 346 Ma extrusion of the SHO rocks in this study. Moreover, this model is inconsistent because a post-collisional event should have begun with a developed crustal anatexis episode that yields peraluminous granitoids and related volcanic rocks followed by a K-enriched magmatic event (Bonin, 2004). However, there is no geological evidence to prove the existence of such Early Carboniferous peraluminous magmatic suites or related volcanic rocks in the southern Yili terrane.

Geochemical studies of modern arc-related magmatism have shown that Ba/La and Ba/Nb ratios can be used as indicators of the total slab-derived input into a mantle wedge. Carr *et al.* (1990) observed a correlation between the Ba/La ratios of arc lavas and the subduction angle along the Central American arc. They attributed the low Ba/La ratios to metasomatism of a larger volume of the overlying mantle wedge during shallow subduction, thereby giving a less pronounced subduction signature. The significantly

higher Ba/La ratios of the K-rich SHO samples imply that their generation is associated with a steepening angle of the subducting slab. The Ba/Nb ratio also provides an indicator of the amount of fluid in the mantle source region, which is a rough proxy for the water content. In contrast to the geochemical data for the Devonian to Carboniferous magmatic rocks, the Early Carboniferous (350–340 Ma) rocks show a consistent variation of their potassium index (K1) and their Ba/La and Ba/Nb ratios that indicates the K-enriched magmatic event had a close relationship to the input of material from the subducted slab (Fig. 13). In terms of the Hf isotopes, the magmatic rocks of Yili terrane have changing $\epsilon_{\text{Hf}}(t)$ values with time, i.e. the evolutionary trend changed from upward to downward (the shift occurred at c. 345 Ma). Further, the spatial-temporal distribution and geochemical characteristics of the late-stage arc magmatism during the Early to Late Carboniferous throughout the Yili terrane suggest that both the northward movement of arc-related magmatism and the increasingly depleted isotopic characteristics (Fig. 14) may be related to the retreat of the Junggar oceanic plate (Cao *et al.* 2017). Moreover, the formation of the Early Carboniferous granites and Late Carboniferous gabbros found in the Baluntai district are more likely related to the rollback of the subducted Palaeo-Junggar Ocean rather than to post-collisional break-off (Yin *et al.* 2016). In this study, the coeval SHO rocks probably formed in an extensional setting that is related to slab rollback of the Junggar oceanic crust. The angle of the subducted slab below the Yili terrane may have changed, allowing for increased fluid input to the mantle wedge or even further asthenospheric interactions. The flow of hot mantle material led to the partial melting of previously metasomatized lithospheric mantle that contained amphibole-bearing veins, thereby forming the K-rich mafic magma responsible for the SHO rocks. Therefore, we infer that the geodynamic setting of the Yili terrane was transformed from a compressional to an extensional regime induced by the rollback of the oceanic slab that began in the Early Carboniferous.

Based on a previously proposed tectonic model and the findings herein, the petrogenesis of the SHO rocks in the southern Yili terrane is as follows. First, normal subduction probably began during the Devonian to Early Carboniferous when the 417–350 Ma calc-alkaline volcanic rocks and I-type granites were formed in the northern Yili terrane. The arrival of a buoyant oceanic plateau at c. 350 Ma began to flatten the slab. Next, at c. 346 Ma, the flat slab underwent rollback toward the north, resulting in the northward-younging of Late Carboniferous magmatism in the Awulale mountain region (Figs 14 and 15). The slab rollback caused increased fluid input into the mantle wedge as well as minor asthenospheric mantle upwelling (Figs 14 and 15), which triggered partial melting in the metasomatized lithospheric mantle above it and produced the Early Carboniferous SHO magmatism in the southern Yili terrane.

6. Conclusions

This work documents the existence of a 346 Ma shoshonite (SHO) suite in the Early Carboniferous Dahalajunshan Volcanic Formation of the southern Yili terrane. These SHO rocks are characterized by low SiO₂ and high potassium contents. Their geochemical features suggest that the parental mafic magma was derived from partial melting of a previously metasomatized sub-continental lithospheric mantle. A review of the geochemical results from the region's Devonian to Carboniferous magmatic rocks reveals that the K-enriched SHO magmatic event had a close

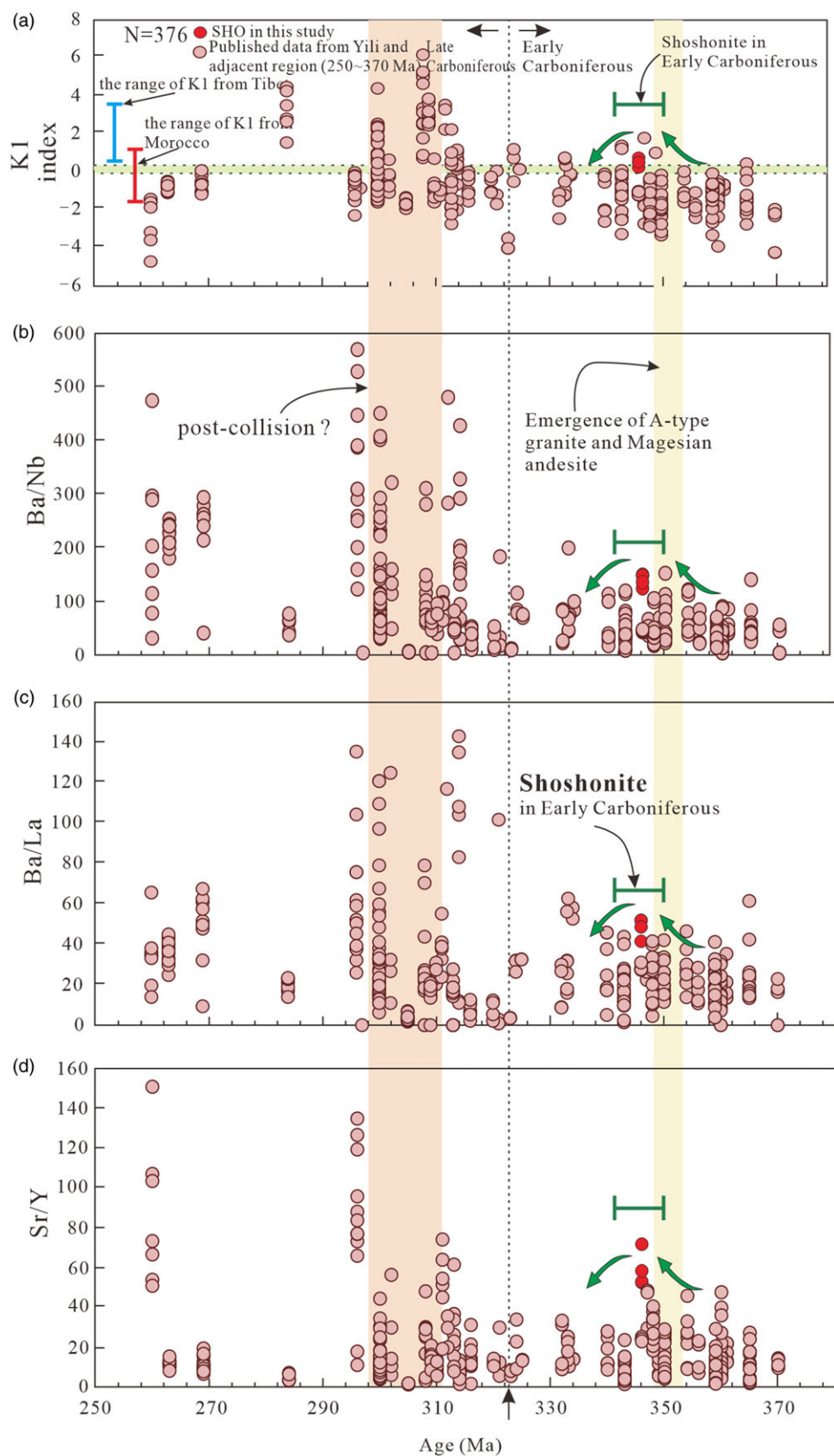


Fig. 13. (Colour online) (a) Potassic index (K1) plotted against age, showing that the highly potassic magmatic activity mainly belongs to two eras, the Early Carboniferous (350–340 Ma) and the Late Carboniferous period (≤ 310 Ma). K1 index is given by $K1 = K_2O - 0.145(SiO_2) + 5.135$, and the field of $K1 > 0$ belongs to the shoshonite series (Manley *et al.* 2000); (b) Ba/Nb vs age (Ma). (c) Ba/La vs age (Ma); (d) Sr/Y vs age (Ma). Data from the shoshonitic samples from Tibet are from Campbell *et al.* (2014), and from the Morocco shoshonitic rocks are from Gill *et al.* (2004).

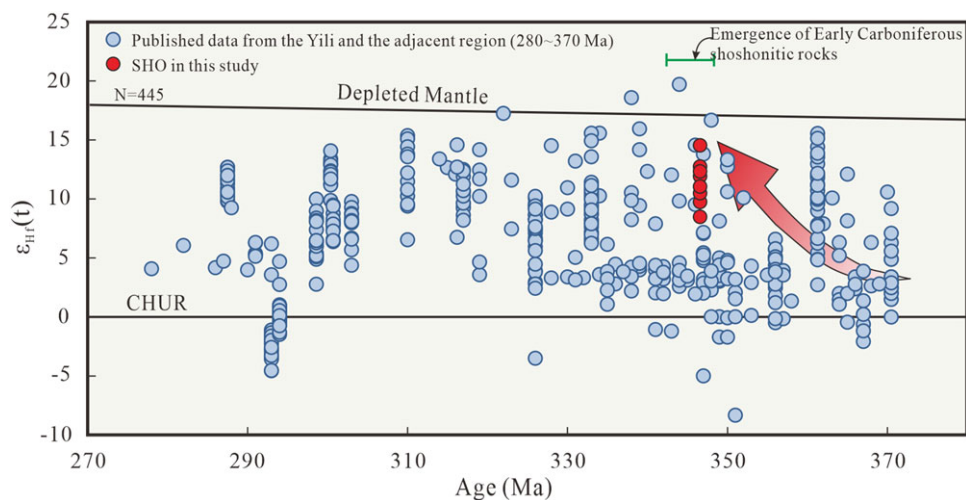


Fig. 14. (Colour online) Plot of $\epsilon_{\text{Hf}}(t)$ values vs U–Pb ages of zircons from the Late Palaeozoic magmatic rocks in the Yili and adjacent region. Notations for the chondritic uniform reservoir (CHUR) and for the depleted mantle (DM) curves are given. Data are from this study (SHO) and previous published studies.

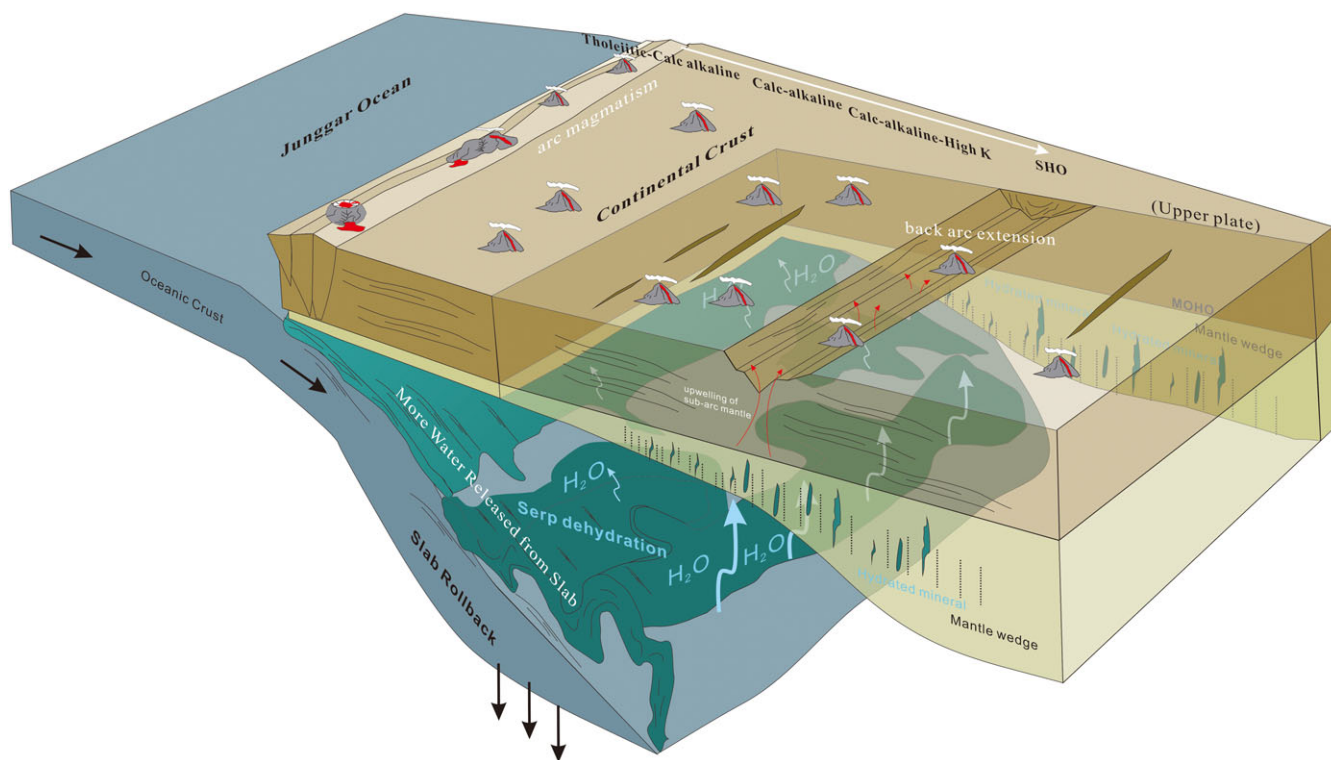


Fig. 15. (Colour online) Sketch model showing the Early Carboniferous tectonic evolution of the Yili terrane and the formation of the shoshonitic rocks in the south of Xinyuan district. The rollback of the Junggar oceanic slab caused the extensional strain in the upper plate and the partial melting of the previously metasomatized mantle wedge that produced the shoshonitic rocks.

relationship to the tectonic attitude of the subduction system. Further, these SHO rocks were likely formed during the rollback of the subducting flat slab, which was responsible for the input of the additional material content.

Supplementary material. To view supplementary material for this article, please visit <https://doi.org/10.1017/S0016756822001303>

Acknowledgements. This study was jointly supported by the National Natural Science Foundation of China (42102061, 42102102), the National

Key Research and Development Program of China (2017YFC0601202), the Fundamental Research Funds for the Central Universities (2652019044) and Jiangxi Provincial Natural Science Foundation (20202BABL213031). CX acknowledges funding under Department of Human Resources and Social Security of Xinjiang Uygur Autonomous Region Introduced Project “Tianchi talent”. We thank three anonymous reviewers for their constructive comments and suggestions.

Declaration of interests. The authors declare that they have no known competing financial interests or personal relationships that could have appeared to influence the work reported in this paper.

Highlights. Early Carboniferous basaltic trachyandesitic tuffs at Xinyuan of the southern Yili terrane have a shoshonitic geochemical affinity.

These basaltic trachyandesitic tuffs were formed by partial melting of metasomatized lithospheric mantle.

The southern Yili terrane have an extensional setting during Early Carboniferous.

References

- Altherr R, Holl A, Hegner E, Langer C and Kreuzer H** (2000) High-potassium, calc-alkaline I-type plutonism in the European variscides: northern Vosges (France) and northern Schwarwald (Germany). *Lithos* **50**, 51–73.
- An F, Zhu YF, Wei SN and Lai SC** (2013) An Early Devonian to Early Carboniferous volcanic arc in North Tianshan, NW China: geochronological and geochemical evidence from volcanic rocks. *Journal of Asian Earth Sciences* **78**, 100–13.
- Andersen T** (2002) Correction of common Pb in U-Pb analyses that do not report ^{204}Pb . *Chemical Geology* **192**, 59–79.
- Avanzinelli R, Lustrino M, Mattei M, Melluso L and Conticelli S** (2009) Potassic and ultrapotassic magmatism in the circum-Tyrrhenian region: significance of carbonated pelitic vs. pelitic sediment recycling at destructive plate margins. *Lithos* **113**, 213–27.
- Beccaluva L, Bianchini G, Mameli P and Natali C** (2013) Miocene shoshonite volcanism in Sardinia: implications for magma sources and geodynamic evolution of the central-western Mediterranean. *Lithos* **180–181**, 128–37.
- Blichert-Toft J and Albarède F** (1997) The Lu-Hf isotope geochemistry of chondrites and the evolution of the mantle-crust system. *Earth and Planetary Science Letters* **148**, 243–58.
- Bonin B** (2004) Do coeval mafic and felsic magmas in post-collisional to within-plate regimes necessarily imply two contrasting, mantle and crustal, sources? A review. *Lithos* **78**, 1–24.
- Campbell IH, Stepanov AS, Liang HY, Allen CM, Norman MC, Zhang YQ and Xie YW** (2014) The origin of shoshonites: new insights from the Tertiary high-potassic intrusions of eastern Tibet. *Lithos* **167**, 1–22.
- Cao YC, Wang B, Jahn BM, Cluzel D, Shu LS and Zhong LL** (2017) Late Paleozoic arc magmatism in the southern Yili Block (NW China): insights to the geodynamic evolution of the Balkhash-Yili continental margin, Central Asian Orogenic Belt. *Lithos* **278–281**, 111–25.
- Carr MJ, Feigenson MD and Bennett EA** (1990) Incompatible element and isotopic evidence for tectonic control of source mixing and melt extraction along the Central American arc. *Contributions to Mineralogy and Petrology* **105**, 369–80.
- Castillo PR, Janney PE and Solidum RU** (1999) Petrology and geochemistry of Camiguin Island, southern Philippines: insights to the source of adakites and other lavas in a complex arc setting. *Contributions to Mineralogy and Petrology* **134**, 33–51.
- Castro A, Aghazadeh M, Badrzadeh Z and Chichorro M** (2013) Late Eocene-Oligocene post-collisional monzonitic intrusions from the Alborz magmatic belt, NW Iran: an example of monzonite magma generation from a metasomatized mantle source. *Lithos* **180–181**, 109–27.
- Chappell BW** (1999) Aluminium saturation in I- and S-type granites and the characterization of fractionated haplogranites. *Lithos* **46**, 535–51.
- Collins W, Beams S, White A and Chappell B** (1982) Nature and origin of A-type granites with particular reference to southeastern Australia. *Contributions to Mineralogy and Petrology* **80**, 189–200.
- Cullen JT, Field MPM and Sherrell RM** (2001) Determination of trace elements in filtered suspended marine particulate material by sector field HR-ICP-MS. *Journal of Analytical Atomic Spectrometry* **16**, 1307–12.
- Defant MJ and Kepezhinkas P** (2001) Evidence suggests slab melting in arc magmas. *Eos, Transactions of the American Geophysical Union* **82**, 65–9.
- Dufek J and Bergantz GW** (2005) Lower crustal magma genesis and preservation: a stochastic framework for the evaluation of basalt-crust interaction. *Journal of Petrology* **46**, 2167–95.
- Feng WY and Zhu YF** (2019) Petrogenesis and tectonic implications of the Late Carboniferous calc-alkaline and shoshonitic magmatic rocks in the Awulale mountain, western Tianshan. *Gondwana Research* **76**, 44–61.
- Feng WY and Zhu YF** (2020) Petrology and geochemistry of Early Carboniferous volcanic rocks in the Xinyuan region of western Tianshan: implications for magma sources. *Lithos* **364–365**, 105550.
- Foley S** (1992) Vein-plus-wall-rock melting mechanisms in the lithosphere and the origin of potassic alkaline magmas. *Lithos* **28**, 435–53.
- Gao J, Long LL, Qian Q, Huang DZ, Su W and Klemd R** (2006) South Tianshan: a Late Paleozoic or Triassic orogen? *Acta Petrologica Sinica* **22**, 1049–61.
- Gill RCO, Aparicio A, El Azzouzi M, Hernandez J, Thirlwall MF, Bourgeois J and Marriner GF** (2004) Depleted arc volcanism in the Alboran Sea and shoshonitic volcanism in Morocco: geochemical and isotopic constraints on Neogene tectonic processes. *Lithos* **78**, 363–88.
- Han YG and Zhao GC** (2018) Final amalgamation of the Tianshan and Junggar orogenic collage in the southwestern Central Asian Orogenic Belt: constraints on the closure of the Paleo-Asian Ocean. *Earth-Science Reviews* **186**, 129–52.
- Hermann J and Rubatto D** (2009) Accessory phase control on the trace element signature of sediment melts in subduction zones. *Chemical Geology* **265**, 512–26.
- Hoskin PWO and Schaltegger U** (2003) The composition of zircon and igneous and metamorphic petrogenesis. *Reviews in Mineralogy and Geochemistry* **53**, 27–62.
- Hou KJ, Li YH, Zou TR, Qu XM, Shi YR and Xie GQ** (2007) Laser ablation-MCICP-MS technique for Hf isotope microanalysis of zircon and its geological applications. *Acta Petrologica Sinica* **23**, 2595–604 (in Chinese with English abstract).
- Huang H, Wang T, Tong Y, Qin Q, Ma XX and Yin JY** (2020) Rejuvenation of ancient micro-continents during accretionary orogenesis: insights from the Yili Block and adjacent regions of the SW Central Asian Orogenic Belt. *Earth-Science Reviews* **208**, 103–255.
- Jackson SE, Pearson NJ, Griffin WL and Belousova EA** (2004) The application of laser ablation-inductively coupled plasma-mass spectrometry to in situ U-Pb zircon geochronology. *Chemical Geology* **211**, 47–69.
- Kay RW and Kay SM** (1993) Delamination and delamination magmatism. *Tectonophysics* **219**, 177–89.
- Kelemen PB, Hanghøj K and Greene AR** (2003) One view of the geochemistry of subduction-related magmatic arcs, with an emphasis on primitive andesite and lower crust. *Treatise on Geochemistry* **3**, 593–659.
- Keskin M, Genç ŞC and Tüysüz O** (2008) Petrology and geochemistry of post-collisional Middle Eocene volcanic units in North-Central Turkey: evidence for magma generation by slab breakoff following the closure of the Northern Neotethys Ocean. *Lithos* **104**, 267–305.
- Lee CTA and Bachmann O** (2014) How important is the role of crystal fractionation in making intermediate magmas? Insights from Zr and P systematics. *Earth and Planetary Science Letters* **393**, 266–74.
- Li HK, Geng JZ, Hao S, Zhang YQ and Li HM** (2009) Determination of U-Pb isotopic age of zircon by Laser ablation multi receiver plasma mass spectrometer (LA-MC-ICPMS). *Acta Mineralogica Sinica* **29**, 600–1 (in Chinese).
- Li JL, Qian Q, Gao J, Su W, Zhang X, Liu X and Jiang T** (2010) Geochemistry zircon U-Pb ages and tectonic settings of the Dahalajunshan volcanics and granitic intrusions from the Adengtao area in the southeast Zhaosu, western Tianshan Mountains. *Acta Petrologica Sinica* **26**, 2913–24 (in Chinese with English abstract).
- Li JL, Su W, Zhang X and Liu X** (2009) Zircon Cameca U-Pb dating and its significance for granulite-facies gneisses from the western Awulale Mountains, Western Tianshan, China. *Geological Bulletin of China* **28**, 1852–62 (in Chinese with English abstract).
- Li WX, Li XH, Wang XC and Yang DS** (2017) Petrogenesis of Cretaceous shoshonitic rocks in the northern Wuyi Mountains, South China: a result of the roll-back of a flat-slab? *Lithos* **288–289**, 125–42.
- Liu YS, Gao S, Hu ZC, Gao CG, Zong KQ and Wang DB** (2010) Continental and oceanic crust recycling-induced melt-peridotite interactions in the Trans-North China orogeny: U-Pb dating, Hf isotopes and trace elements in zircons of mantle xenoliths. *Journal of Petrology* **51**, 537–71.
- Long LL, Gao J, Klemd R, Beier C, Qian Q, Zhang X, Wang JB and Jiang T** (2011) Geochemical and geochronological studies of granitoid rocks from

- the Western Tianshan Orogen: implications for continental growth in the southwestern Central Asian Orogenic Belt. *Lithos* **126**, 321–40.
- Long LL, Gao J, Xiong XM and Qian Q** (2006) The geochemical characteristics and the age of the Kule Lake ophiolite in the southern Tianshan. *Acta Petrologica Sinica* **22**, 65–73 (in Chinese with English abstract).
- Ludwig KR** (2003) *ISOPLOT 3.00: A Geochronology Toolkit for Microsoft Excel*. Berkeley, California: Berkeley Geochronological Center Special Publication, 53 pp.
- Manley CR, Glazner AF and Farmer GL** (2000) Timing of volcanism in the Sierra Nevada of California: evidence for Pliocene delamination of the batholithic root? *Geology* **28**, 811–14.
- Morrison GW** (1980) Characteristics and tectonic setting of the shoshonitic rock association. *Lithos* **13**, 97–108.
- Omrani J, Agard P, Whitechurch H, Benoit M, Prouteau G and Jolivet L** (2008) Arc-magmatism and subduction history beneath the Zagros Mountains, Iran: a new report of adakites and geodynamic consequences. *Lithos* **106**, 380–98.
- Pe-Piper G, Piper DJW, Koukouvelas I, Dolansky LM and Kokkalas S** (2009) Post-orogenic shoshonitic rocks and their origin by melting underplated basalts: the Miocene of Limnos, Greece. *Geological Society of America Bulletin* **121**, 39–54.
- Petford N and Atherton M** (1996) Na-rich partial melts from newly underplated basaltic crust: the Cordillera Blanca Batholith, Peru. *Journal of Petrology* **37**, 1491–521.
- Portnyagin M, Hoernle K, Plechov P, Mironov N and Khubunaya S** (2007) Constraints on mantle melting and composition and nature of slab components in volcanic arcs from volatiles and trace elements in melt inclusions from the Kamchatka Arc. *Earth and Planetary Science Letters* **255**, 63–9.
- Rapp RP and Watson EB** (1995) Dehydration melting of metabasalt at 8–32 kbar: implications for continental growth and crust-mantle recycling. *Journal of Petrology* **36**, 891–931.
- Richards JP and Kerrich R** (2007) Special paper. Adakite-like rocks: their diverse origins and questionable role in metallogenesis. *Economic Geology* **102**, 537–76.
- Ru YJ** (2012) The stratigraphic sequence, petrogenesis and tectonic setting of the volcanic rocks of the Dahalajunshan Formation, western Tianshan Mountain, China. Master degree of Chang'an University, pp. 1–113 (in Chinese with English abstract).
- Saunders AD, Rogers G, Marriner GF, Terrell DJ and Verma SP** (1987) Geochemistry of Cenozoic volcanic rocks, Baja California, Mexico: implications for the petrogenesis of post-subduction magmas. *Journal of Volcanology and Geothermal Research* **32**, 223–45.
- Sisson TW, Ratajeski K, Hankins WB and Glazner AF** (2005) Voluminous granitic magmas from common basaltic sources. *Contributions to Mineralogy and Petrology* **148**, 635–61.
- Söderlund U, Patchett PJ, Vervoort JD and Isachsen CE** (2004) The ^{176}Lu decay constant determined by Lu-Hf and U-Pb isotope systematics of Precambrian mafic intrusions. *Earth and Planetary Science Letters* **219**, 311–24.
- Sun SS and McDonough WF** (1989) Chemical and isotopic systematics of oceanic basalts: implications for mantle composition and processes. In *Magmatism in the Ocean Basins* (eds AD Saunders and MJ Norry), pp. 313–45. Geological Society of London, Special Publication no. 42.
- Tan Z, Agard P, Patrick M, Gao J, John T, Léa B, Jiang T, Wang XS, Hong T, Wan B and Caron B** (2019) Architecture and P-T-deformation-time evolution of the Chinese SW-Tianshan HP/UHP complex: implications for subduction dynamics. *Earth-Science Reviews* **197**, 102894.
- Tarney J and Jones CE** (1994) Trace element geochemistry of orogenic igneous rocks and crustal growth models. *Journal of the Geological Society* **151**, 855–68.
- Taylor SR and McLennan SM** (1985) *The Continental Crust: Its Composition and Evolution*. Oxford: Blackwell.
- Turner S, Arnaud N, Liu J, Rogers N, Hawkesworth C, Harris N, Kelley S, Van Calsteren P and Deng W** (1996) Post-collision, shoshonitic volcanism on the Tibetan Plateau: implications for convective thinning of the lithosphere and the source of Ocean Island Basalts. *Journal of Petrology* **37**, 45–71.
- Turner S, Hawkesworth C, Liu JQ, Rogers N, Kelley S and van Calsteren P** (1993) Timing of Tibetan uplift constrained by analysis of volcanic rocks. *Nature* **364**, 50–4.
- Vigouroux N, Wallace PJ and Kent AJR** (2008) Volatiles in high-K magmas from the western Trans-Mexican Volcanic Belt: evidence for fluid fluxing and extreme enrichment of the mantle wedge by subduction processes. *Journal of Petrology* **49**, 12–5.
- Wang B, Chen Y, Zhan S, Shu LS, Michel F, Cluzel D, Charvet J and Laurent-Charvet S** (2007) Primary Carboniferous and Permian paleomagnetic results from the Yili Block (NW China) and their implications on the geodynamic evolution of Chinese Tianshan Belt. *Earth and Planetary Science Letters* **263**, 288–308.
- Wang B, Cluzel D, Shu LS, Faure M, Charvet J, Chen Y, Meffre S and de Jong K** (2009) Evolution of calc-alkaline to alkaline magmatism through Carboniferous convergence to Permian transcurrent tectonics, western Chinese Tianshan. *International Journal of Earth Science* **98**, 1275–98.
- Wang B, Liu HS, Shu LS, Jahn BM, Chung SL, Zhai YZ and Liu DY** (2014) Early Neoproterozoic crustal evolution in northern Yili Block: insights from migmatite, orthogneiss and leucogranite of the Wenquan metamorphic complex in the NW Chinese Tianshan. *Precambrian Research* **242**, 58–81.
- Wang W, Zeng LS, Gao LE, Wang Q, Guo C, Hou KJ and Zeng JL** (2018) Eocene-Oligocene potassic high Ba-Sr granitoids in the Southeastern Tibet: petrogenesis and tectonic implications. *Lithos* **322**, 38–51.
- Wang ZP, Li YJ, Yang GX, Tong LL, Li H, Luo YQ and Liu Y** (2020) Petrogenesis and geochemical characteristics of Early Carboniferous sanukitic high-Mg andesite from Atengtao Mountain, Yili Block: implications for the tectonic setting during Late Paleozoic in Chinese West Tianshan. *Geological Journal* **55**, 517–32.
- Windley BF, Alexeiev D, Xiao WJ, Kroner A and Badarch G** (2007) Tectonic models for accretion of the Central Asian Orogenic Belt. *Journal of the Geological Society* **164**, 31–47.
- XBGMR (Xinjiang Bureau of Geology and Mineral Resources)** (1993) *Regional Geology of Xinjiang Uygur Autonomy Region*. Beijing: Geology Publishing House, 841 pp. (in Chinese with English abstract).
- Xia LQ and Li XM** (2020) Revisiting the tectonic setting of the Carboniferous volcanic rocks in the Chinese Tianshan and its neighboring areas. *Gondwana Research* **84**, 1–19.
- Xia LQ, Xu XY, Li XM, Ma ZP and Xia ZC** (2012) Reassessment of petrogenesis of Carboniferous-Early Permian rift-related volcanic rocks in the Chinese Tianshan and its neighboring areas. *Geoscience Frontiers* **3**, 445–71.
- Xing H, Xue CJ, Chi GX, Zhao XB, Liu C, Man RH and Symons DTA** (2021) Petrogenesis of volcanic rocks of the Devonian-Carboniferous Dahalajunshan Formation, Western Tianshan: implications for crustal growth in an accretionary orogen. *Lithos* **386–387**, 106003.
- Xu XY, Li XM, Ma ZP, Xia LQ, Xia ZC and Pen GX** (2006) LA-ICP-MS zircon U-Pb dating of gabbro from the Bayingou ophiolite in the northern Tianshan Mountains. *Acta Geologica Sinica* **80**, 1168–76.
- Xu XY, Wang HL, Li P, Chen JL, Ma ZP, Zhu T, Wang N and Dong YP** (2013) Geochemistry and geochronology of Paleozoic intrusions in the Nalati (Narati) area in western Tianshan, Xinjiang, China: implications for Paleozoic tectonic evolution. *Journal of Asian Earth Sciences* **72**, 33–62.
- Yang WB, Niu HC, Shan Q, Luo Y, Sun WD, Li CY, Li NB and Yu XY** (2012) Late Paleozoic calc-alkaline to shoshonitic magmatism and its geodynamic implications, Yuximolegai area, western Tianshan, Xinjiang. *Gondwana Research* **22**, 325–40.
- Yin JY, Chen W, Xiao WJ, Yuan C, Zhang B, Cai KD and Long XP** (2016) Geochronology, petrogenesis and tectonic significance of the Latest Devonian-Early Carboniferous I-type granites in the Central Tianshan, NW China. *Gondwana Research* **47**, 188–99.
- Yu XQ, Wang ZX, Zhou X, Xiao WF and Yang XP** (2016) Zircon U-Pb geochronology and Sr-Nd isotopes of volcanic rocks from the Dahalajunshan Formation: implications for Late Devonian–Middle Carboniferous tectonic evolution of the Chinese Western Tianshan. *International Journal of Earth Sciences* **105**, 1637–61.
- Zhao XB, Xue CJ, Chi GX, Wang HG and Qi TJ** (2014) Epithermal Au and polymetallic mineralization in the Tulasu Basin, western Tianshan, NW China: potential for the discovery of porphyry Cu-Au deposits. *Ore Geology Reviews* **60**, 76–96.

- Zhao ZH, Bai ZH, Xiong XL, Mei HJ and Wang YX** (2003) $^{40}\text{Ar}/^{39}\text{Ar}$ chronological study of Late Paleozoic volcanic-hypabyssal igneous rocks in western Tianshan, Xinjiang. *Geochemica* **32**, 317–27 (in Chinese with English abstract).
- Zhu YF, An F, Xue YX, Chen B and Zhang LF** (2010) Zircon U-Pb age for Kesang Rondong volcanic rocks, Southwest Tianshan Mts, Tekes, Xinjiang. *Acta Petrologica Sinica* **26**, 2255–63 (in Chinese with English abstract).
- Zhu YF, Guo X, Song B, Zhang LF and Gu LB** (2009) Petrology, Sr-Nd-Hf isotopic geochemistry and zircon chronology of the Late Paleozoic volcanic rocks in the southwestern Tianshan Mountains, Xinjiang, NW China. *Journal of the Geological Society* **166**, 1085–99.
- Zhu YF, Zhang LF, Gu LB, Guo X and Zhou J** (2005) Study on trace element geochemistry and SHRIMP chronology of Carboniferous volcanic rocks in Western Tianshan. *Chinese Science Bulletin* **50**, 2004–14 (in Chinese).
- Zu B, Seltmann R, Xue CJ, Wang T, Dolgoplova A, Li C, Zhou LM, Pak N, Ivleva E, Chai MC and Zhao XB** (2019) Multiple episodes of Late Paleozoic Cu-Au mineralization in the Chatkal-Kurama terrane: new constraints from the Kuru-Tegerek and Bozymchak skarn deposits, Kyrgyzstan. *Ore Geology Reviews* **113**, 103077.